LHCb-CONF-2015-002
March 23, 2015

Angular analysis of the $B^0 \to K^{*0}\mu^+\mu^-$ decay

The LHCb collaboration [†]

Abstract

An angular analysis of the $B^0 \to K^{*0}\mu^+\mu^-$ decay is presented using pp-collision data collected at the LHCb experiment. The dataset corresponds to an integrated luminosity of $3\,\text{fb}^{-1}$. The analysis uses the full angular distribution and measures all CP-averaged angular observables and the correlations between these observables, taking into account the contamination from $K^+\pi^-$ in an S-wave configuration.

Neglecting the correlations between the observables, the measurements are largely in agreement with the Standard Model predictions. However, the observable P_5' exhibits a local tension with respect to the Standard Model prediction at a level of 3.7σ.

[†]Conference report prepared for the 50th rencontres de Moriond on electroweak interactions and unified theories. Contact authors: Christoph Langenbruch christoph.langenbruch@cern.ch, Kostas Petridis konstantinos.petridis@cern.ch and Nicola Serra nicola.serra@cern.ch.

1 Introduction

The decay $B^0 \to K^{*0}(\to K^+\pi^-)\mu^+\mu^-$ proceeds via a b- to s-quark flavour changing neutral current (FCNC) transition.[1] In the Standard Model (SM) the decay is therefore forbidden at tree level and, at lowest order, only occurs via electroweak penguin and box processes. In extensions of the SM, new, heavy particles can enter in competing processes and can significantly change the branching fraction of the decay and the angular distribution of the final state particles. Angular observables are of particular interest, since theoretical predictions of such observables tend to be less affected by form-factor uncertainties in the $B^0 \to K^{*0}$ transition. Hereafter, K^{*0} is used to refer to the $K^{*0}(892)$.

The LHCb collaboration previously determined a range of angular observables in the $B^0 \to K^{*0}\mu^+\mu^-$ decay, using data collected during 2011, corresponding to an integrated luminosity of $1\,\text{fb}^{-1}$ [1]. Different subsets of these angular observables have also been measured by the BaBar, Belle, CDF, ATLAS and CMS collaborations [2–6] and all of these measurements are in good agreement with SM predictions. The LHCb collaboration has also used the 2011 dataset to determine a separate set of angular observables that have reduced theoretical uncertainties [7]. In contrast to the previous analyses, these observables cannot be extracted from single angle projections. This second LHCb analysis found a local deviation with respect to the SM prediction, with a significance corresponding to 3.7σ in one observable, P_5'. Possible interpretations of this discrepancy and the consistency of all of the measurements of $b \to s$ transitions have been widely discussed in the literature [8–20].

The present note describes an updated angular analysis of the $B^0 \to K^{*0}\mu^+\mu^-$ decay, using the full LHCb Run I data sample, corresponding to an integrated luminosity of $3\,\text{fb}^{-1}$. The data were taken at centre-of-mass energies of 7 and 8 TeV during 2011 and 2012, respectively. All previous analyses of the $B^0 \to K^{*0}\mu^+\mu^-$ decay have determined some subset of the information available by fitting a simplified form of the angular distribution. Using the full angular distribution, the present note extracts a complete set of CP-averaged observables for the first time. The simultaneous extraction of these observables enables the correlations between the measured quantities to be computed, enabling the observables to be included in global fits to theoretical models in a statistically correct way. This is critical to understand whether SM dynamics are sufficient to explain the above discrepancy, or if extensions to the SM are necessary.

The structure of this note is as follows. The angular distribution and observables for the $B^0 \to K^{*0}\mu^+\mu^-$ decay are first presented in Section 2. Section 3 then describes the experimental setup. The reconstruction and selection of the $B^0 \to K^{*0}\mu^+\mu^-$ candidates and sources of background are presented in Section 4. The method used to correct the angular distribution for experimental effects is detailed in Section 5 and the parameterisation of the mass distribution is described in Section 6. Section 7 describes the extraction of the angular observables and Section 8 the systematic uncertainties. Results are presented in Section 9. Finally, conclusions are presented in Section 10.

[1] Charge conjugation is implied throughout this note unless otherwise noted.

2 Angular distribution and observables

The final state of the decay $B^0 \to K^{*0}\mu^+\mu^-$ can be fully described by q^2, the invariant mass of the dimuon system squared, and three decay angles $\vec{\Omega} = (\cos\theta_l, \cos\theta_K, \phi)$. The angle θ_l denotes the angle between the μ^+ (μ^-) and the direction opposite the B^0 ($\overline{B}^0$) in the rest frame of the dimuon system. The angle θ_K is defined as the angle between the direction of the K^+ (K^-) and the B^0 ($\overline{B}^0$) in the rest frame of the K^{*0} ($\overline{K}^{*0}$) system. The angle ϕ describes the angle between the plane defined by the μ^+ and μ^- and the plane defined by the kaon and pion in the B^0 ($\overline{B}^0$) rest frame. More details on the angular basis adopted in this analysis are given in Appendix A of Ref. [1].

The differential decay rate of $\overline{B}^0 \to \overline{K}^{*0}\mu^+\mu^-$ and $B^0 \to K^{*0}\mu^+\mu^-$ decays, in terms of q^2 and the three angles, is given by

$$\begin{aligned}\frac{\mathrm{d}^4\Gamma[\overline{B}^0 \to \overline{K}^{*0}\mu^+\mu^-]}{\mathrm{d}q^2\,\mathrm{d}\vec{\Omega}} &= \frac{9}{32\pi}\sum_{j(s,c)} I_{j(s,c)}(q^2) f_j(\vec{\Omega}) \quad \text{and} \\ \frac{\mathrm{d}^4\bar{\Gamma}[B^0 \to K^{*0}\mu^+\mu^-]}{\mathrm{d}q^2\,\mathrm{d}\vec{\Omega}} &= \frac{9}{32\pi}\sum_{j(s,c)} \bar{I}_{j(s,c)}(q^2) f_j(\vec{\Omega}) \quad , \end{aligned} \tag{1}$$

where the terms $f_j(\vec{\Omega})$ arise from spherical harmonics and the $I_{j(s,c)}(q^2)$ are eleven q^2 dependent angular observables. The $I_{j(s,c)}$ can in turn be expressed as bilinear combinations of six complex decay amplitudes, $\mathcal{A}^{\mathrm{L,R}}_{0,\parallel,\perp}$, which correspond to different transversity states of the K^{*0} and different (left- and right-handed) chiralities of the dimuon system. The indices s and c denote terms proportional to $\sin^2\theta_K$ and $\cos^2\theta_K$ and have been kept for comparison to theory. A full list of the angular terms and observables is given in Table 1. Following the notation of Ref. [21], *CP*-averaged observables can be defined as

$$S_j = \left(I_{j(s,c)} + \bar{I}_{j(s,c)}\right) \Big/ \left(\frac{\mathrm{d}\Gamma}{\mathrm{d}q^2} + \frac{\mathrm{d}\bar{\Gamma}}{\mathrm{d}q^2}\right) \quad . \tag{2}$$

If q^2 is sufficiently large ($q^2 \gtrsim 1\,\mathrm{GeV}^2/c^4$), the muons can be considered massless and the *CP*-averaged observables $S_{1(s,c)}$ and $S_{2(s,c)}$ obey the relations $S_{1s} = 3S_{2s}$, $S_{1c} = -S_{2c}$ and $\frac{3}{4}(2S_{1s} + S_{1c}) - \frac{1}{4}(2S_{2s} + S_{2c}) = 1$ (see for example Ref. [21]). These relationships reduce the number of observables from eleven to eight. In the present analysis, these relations are also assumed to hold in the region $q^2 < 1\,\mathrm{GeV}^2/c^4$. The S_{1c} observable is more commonly expressed in terms of the longitudinal polarisation fraction of the K^{*0},

$$F_{\mathrm{L}} = S_{1c} = \frac{|\mathcal{A}^{\mathrm{L}}_0|^2 + |\mathcal{A}^{\mathrm{R}}_0|^2}{|\mathcal{A}^{\mathrm{L}}_0|^2 + |\mathcal{A}^{\mathrm{R}}_0|^2 + |\mathcal{A}^{\mathrm{L}}_\parallel|^2 + |\mathcal{A}^{\mathrm{R}}_\parallel|^2 + |\mathcal{A}^{\mathrm{L}}_\perp|^2 + |\mathcal{A}^{\mathrm{R}}_\perp|^2} \ . \tag{3}$$

It is also conventional to replace S_{6s} by the forward-backward asymmetry of the dimuon system A_{FB}, where $A_{\mathrm{FB}} = \frac{3}{4}S_{6s}$. The *CP*-averaged angular distribution of the $B^0 \to$

$K^{*0}\mu^+\mu^-$ signal can therefore be written as

$$\begin{aligned}\frac{1}{\mathrm{d}(\Gamma+\bar{\Gamma})/\mathrm{d}q^2}\frac{\mathrm{d}^3(\Gamma+\bar{\Gamma})}{\mathrm{d}\vec{\Omega}}\bigg|_{\mathrm{P}} = \frac{9}{32\pi}\Big[&\tfrac{3}{4}(1-F_{\mathrm{L}})\sin^2\theta_K + F_{\mathrm{L}}\cos^2\theta_K \\ &+\tfrac{1}{4}(1-F_{\mathrm{L}})\sin^2\theta_K\cos 2\theta_l \\ &-F_{\mathrm{L}}\cos^2\theta_K\cos 2\theta_l + S_3\sin^2\theta_K\sin^2\theta_l\cos 2\phi \\ &+S_4\sin 2\theta_K\sin 2\theta_l\cos\phi + S_5\sin 2\theta_K\sin\theta_l\cos\phi \\ &+\tfrac{4}{3}A_{\mathrm{FB}}\sin^2\theta_K\cos\theta_l + S_7\sin 2\theta_K\sin\theta_l\sin\phi \\ &+S_8\sin 2\theta_K\sin 2\theta_l\sin\phi + S_9\sin^2\theta_K\sin^2\theta_l\sin 2\phi\Big].\end{aligned} \tag{4}$$

Additional sets of observables, for which the leading form-factor uncertainties cancel, can be built from F_{L} and S_3 through S_9. Examples of such "optimised" observables include the transverse asymmetry $A_{\mathrm{T}}^{(2)}$ [22], where $A_{\mathrm{T}}^{(2)} = S_3/(1-F_{\mathrm{L}})$, and the P' series of observables [23], with, for example, $P'_{4,5} = S_{4,5}/\sqrt{F_{\mathrm{L}}(1-F_{\mathrm{L}})}$.

At LHCb, the K^{*0} is reconstructed through the decay $K^{*0}\to K^+\pi^-$. In addition to the resonant P-wave K^{*0} contribution to the $K^+\pi^-\mu^+\mu^-$ final state, the $K^+\pi^-$ can also be in an S-wave configuration. The addition of an S-wave component introduces two new complex amplitudes, $\mathcal{A}_{\mathrm{S}}^{L,R}$, and results in six additional angular terms. The new angular terms are given in the lower part of Table 1. In the analyses described in Refs [1, 7] the S-wave pollution, which is expected to be on the order of ten percent, was treated as a systematic uncertainty. The introduction of a $K^+\pi^-$ system in an S-wave configuration modifies the angular distribution to

$$\begin{aligned}\frac{1}{\mathrm{d}(\Gamma+\bar{\Gamma})/\mathrm{d}q^2}\frac{\mathrm{d}^3(\Gamma+\bar{\Gamma})}{\mathrm{d}\vec{\Omega}}\bigg|_{\mathrm{S+P}} &= (1-F_{\mathrm{S}})\,\frac{1}{\mathrm{d}(\Gamma+\bar{\Gamma})/\mathrm{d}q^2}\frac{\mathrm{d}^3(\Gamma+\bar{\Gamma})}{\mathrm{d}\vec{\Omega}}\bigg|_{\mathrm{P}} \\ &\quad + \frac{3}{16\pi}F_{\mathrm{S}}\sin^2\theta_\ell \;+\; \text{S-P interference}\end{aligned} \tag{5}$$

where F_{S} denotes the S-wave fraction and S-P interference refers to the terms in Table 1 that depend on both the P- and S-wave amplitudes.

For the present analysis, an unbinned maximum likelihood fit is used to determine the *CP*-averaged observables F_{L}, A_{FB}, and S_3 through S_9. The S-wave observables are explicitly included as nuisance parameters. The data are analysed in approximately $2\,\mathrm{GeV}^2/c^4$ q^2 bins and measurements are also made in wider $1.1 < q^2 < 6.0\,\mathrm{GeV}^2/c^4$ and $15.0 < q^2 < 19.0\,\mathrm{GeV}^2/c^4$ bins for which there are particularly precise theoretical predictions (see Tables 2 and 3 for details).

3 Detector and simulation

The LHCb detector [24,25] is a single-arm forward spectrometer covering the pseudorapidity range $2 < \eta < 5$, designed for the study of particles containing b- or c-quarks. The detector

Table 1: Angular observables I_j and their corresponding angular terms for dimuon masses that are much larger than twice the muon mass. The terms below the line only arise in the presence of an S-wave contribution to the $K^+\pi^-\mu^+\mu^-$ final state.

j	I_j	f_j
$1s$	$\frac{3}{4}\left[\lvert\mathcal{A}_\parallel^{\rm L}\rvert^2+\lvert\mathcal{A}_\perp^{\rm L}\rvert^2+\lvert\mathcal{A}_\parallel^{\rm R}\rvert^2+\lvert\mathcal{A}_\perp^{\rm R}\rvert^2\right]$	$\sin^2\theta_K$
$1c$	$\lvert\mathcal{A}_0^{\rm L}\rvert^2+\lvert\mathcal{A}_0^{\rm R}\rvert^2$	$\cos^2\theta_K$
$2s$	$\frac{1}{4}\left[\lvert\mathcal{A}_\parallel^{\rm L}\rvert^2+\lvert\mathcal{A}_\perp^{\rm L}\rvert^2+\lvert\mathcal{A}_\parallel^{\rm R}\rvert^2+\lvert\mathcal{A}_\perp^{\rm R}\rvert^2\right]$	$\sin^2\theta_K\cos 2\theta_\ell$
$2c$	$-\lvert\mathcal{A}_0^{\rm L}\rvert^2-\lvert\mathcal{A}_0^{\rm R}\rvert^2$	$\cos^2\theta_K\cos 2\theta_\ell$
3	$\frac{1}{2}\left[\lvert\mathcal{A}_\perp^{\rm L}\rvert^2-\lvert\mathcal{A}_\parallel^{\rm L}\rvert^2+\lvert\mathcal{A}_\perp^{\rm R}\rvert^2-\lvert\mathcal{A}_\parallel^{\rm R}\rvert^2\right]$	$\sin^2\theta_K\sin^2\theta_\ell\cos 2\phi$
4	$\sqrt{\frac{1}{2}}\mathrm{Re}(\mathcal{A}_0^{\rm L}\mathcal{A}_\parallel^{\rm L*}+\mathcal{A}_0^{\rm R}\mathcal{A}_\parallel^{\rm R*})$	$\sin 2\theta_K\sin 2\theta_\ell\cos\phi$
5	$\sqrt{2}\mathrm{Re}(\mathcal{A}_0^{\rm L}\mathcal{A}_\perp^{\rm L*}-\mathcal{A}_0^{\rm R}\mathcal{A}_\perp^{\rm R*})$	$\sin 2\theta_K\sin\theta_\ell\cos\phi$
6s	$2\mathrm{Re}(\mathcal{A}_\parallel^{\rm L}\mathcal{A}_\perp^{\rm L*}-\mathcal{A}_\parallel^{\rm R}\mathcal{A}_\perp^{\rm R*})$	$\sin^2\theta_K\cos\theta_\ell$
7	$\sqrt{2}\mathrm{Im}(\mathcal{A}_0^{\rm L}\mathcal{A}_\parallel^{\rm L*}-\mathcal{A}_0^{\rm R}\mathcal{A}_\parallel^{\rm R*})$	$\sin 2\theta_K\sin\theta_\ell\sin\phi$
8	$\sqrt{\frac{1}{2}}\mathrm{Im}(\mathcal{A}_0^{\rm L}\mathcal{A}_\perp^{\rm L*}+\mathcal{A}_0^{\rm R}\mathcal{A}_\perp^{\rm R*})$	$\sin 2\theta_K\sin 2\theta_\ell\sin\phi$
9	$\mathrm{Im}(\mathcal{A}_\parallel^{\rm L*}\mathcal{A}_\perp^{\rm L}+\mathcal{A}_\parallel^{\rm R*}\mathcal{A}_\perp^{\rm R})$	$\sin^2\theta_K\sin^2\theta_\ell\sin 2\phi$
10	$\frac{1}{3}\left[\lvert\mathcal{A}_{\rm S}^{\rm L}\rvert^2+\lvert\mathcal{A}_{\rm S}^{\rm R}\rvert^2\right]$	1
11	$\sqrt{\frac{4}{3}}\mathrm{Re}(\mathcal{A}_{\rm S}^{\rm L}\mathcal{A}_0^{\rm L*}+\mathcal{A}_{\rm S}^{\rm R}\mathcal{A}_0^{\rm R*})$	$\cos\theta_K$
12	$-\frac{1}{3}\left[\lvert\mathcal{A}_{\rm S}^{\rm L}\rvert^2+\lvert\mathcal{A}_{\rm S}^{\rm R}\rvert^2\right]$	$\cos 2\theta_\ell$
13	$-\sqrt{\frac{4}{3}}\mathrm{Re}(\mathcal{A}_{\rm S}^{\rm L}\mathcal{A}_0^{\rm L*}+\mathcal{A}_{\rm S}^{\rm R}\mathcal{A}_0^{\rm R*})$	$\cos\theta_K\cos 2\theta_\ell$
14	$\sqrt{\frac{2}{3}}\mathrm{Re}(\mathcal{A}_{\rm S}^{\rm L}\mathcal{A}_\parallel^{\rm L*}+\mathcal{A}_{\rm S}^{\rm R}\mathcal{A}_\parallel^{\rm R*})$	$\sin\theta_K\sin 2\theta_\ell\cos\phi$
15	$\sqrt{\frac{8}{3}}\mathrm{Re}(\mathcal{A}_{\rm S}^{\rm L}\mathcal{A}_\perp^{\rm L*}-\mathcal{A}_{\rm S}^{\rm R}\mathcal{A}_\perp^{\rm R*})$	$\sin\theta_K\sin\theta_\ell\cos\phi$
16	$\sqrt{\frac{8}{3}}\mathrm{Im}(\mathcal{A}_{\rm S}^{\rm L}\mathcal{A}_\parallel^{\rm L*}-\mathcal{A}_{\rm S}^{\rm R}\mathcal{A}_\perp^{\rm R*})$	$\sin\theta_K\sin\theta_\ell\sin\phi$
17	$\sqrt{\frac{2}{3}}\mathrm{Im}(\mathcal{A}_{\rm S}^{\rm L}\mathcal{A}_\perp^{\rm L*}+\mathcal{A}_{\rm S}^{\rm R}\mathcal{A}_\perp^{\rm R*})$	$\sin\theta_K\sin 2\theta_\ell\sin\phi$

includes a high-precision tracking system consisting of a silicon-strip vertex detector surrounding the pp interaction region [26], a large-area silicon-strip detector located upstream of a dipole magnet with a bending power of about 4 Tm, and three stations of silicon-strip detectors and straw drift tubes [27] placed downstream of the magnet. The tracking system provides a measurement of momentum, p, of charged particles with a relative uncertainty that varies from 0.5% at low momentum to 1.0% at 200 GeV/c. The minimum distance of a track to a primary pp interaction vertex (PV), the impact parameter, is measured with a resolution of $(15+29/p_{\rm T})\,\mu$m, where $p_{\rm T}$ is the component of the momentum transverse to the beam, in GeV/c. Different types of charged hadrons are distinguished using information from two ring-imaging Cherenkov (RICH) detectors [28].

Photons, electrons and hadrons are identified by a calorimeter system consisting of scintillating-pad and preshower detectors, an electromagnetic calorimeter and a hadronic calorimeter. Muons are identified by a system composed of alternating layers of iron and multiwire proportional chambers [29].

The online event selection is performed by a trigger [30], which consists of a hardware stage, based on information from the calorimeter and muon systems, followed by a software stage, which applies a full event reconstruction.

A large sample of simulated signal events is used to determine the impact of the detector geometry, trigger, reconstruction and candidate selection on the angular distribution of the signal. In addition, simulated samples are used to estimate pollution by possible background processes. In the simulation, pp collisions are generated using Pythia [31] with a specific LHCb configuration [32]. Decays of hadronic particles are described by EvtGen [33], in which final-state radiation is generated using Photos [34]. The interaction of the generated particles with the detector, and its response, are implemented using the Geant4 toolkit [35] as described in Ref. [36]. Data-driven corrections are applied to the simulation to account for the small level of mismodelling of the detector occupancy, B^0 momentum and B^0 vertex quality. Similarly, the simulated particle identification (PID) performance is corrected to match the performance determined from control samples selected from the data.

4 Selection of signal candidates

The $B^0 \to K^{*0}\mu^+\mu^-$ signal candidates are first required to pass a hardware trigger, which selects muons with $p_{\rm T} > 1.48\,{\rm GeV}/c$ in the 7 TeV data or $p_{\rm T} > 1.76\,{\rm GeV}/c$ in the 8 TeV data. In the subsequent software trigger, at least one of the final-state particles is required to have both $p_{\rm T} > 0.8\,{\rm GeV}/c$ and impact parameter larger than 100 μm with respect to all of the PVs in the event. Finally, the tracks of two or more of the final-state particles are required to form a vertex that is significantly displaced from the PVs.

Signal candidates are only accepted for further analysis if they pass a loose preselection. The final-state particles are required to have $\chi^2_{\rm IP} > 9$ with respect to all of the PVs in the event, where $\chi^2_{\rm IP}$ is defined as the change in the χ^2 of the PV when reconstructing it with and without the considered particle. The four final-state particles are then fit to a common vertex, which is required to be of good quality (with vertex $\chi^2 < 8$ per degree of freedom). The $\chi^2_{\rm IP}$ of the B^0 candidate with respect to one of the PVs is required to be small ($\chi^2_{\rm IP} < 16$) and the B^0 candidate is required to be significantly displaced from the same PV; the χ^2 for a fit to the PV is required to increase by more than 121 when including the B^0 decay products. Furthermore, the angle $\theta_{\rm DIRA}$ between the reconstructed B^0 momentum and the vector connecting the PV with the reconstructed B^0 decay vertex is required to be smaller than 14 mrad. Candidates are required to have reconstructed B^0 invariant mass, $m(K^+\pi^-\mu^+\mu^-)$, in the range $5170 < m(K^+\pi^-\mu^+\mu^-) < 5700\,{\rm MeV}/c^2$. Finally, the reconstructed mass of the $K^+\pi^-$ system, $m(K^+\pi^-)$, is required to be in the range $795.9 < m(K^+\pi^-) < 995.9\,{\rm MeV}/c^2$.

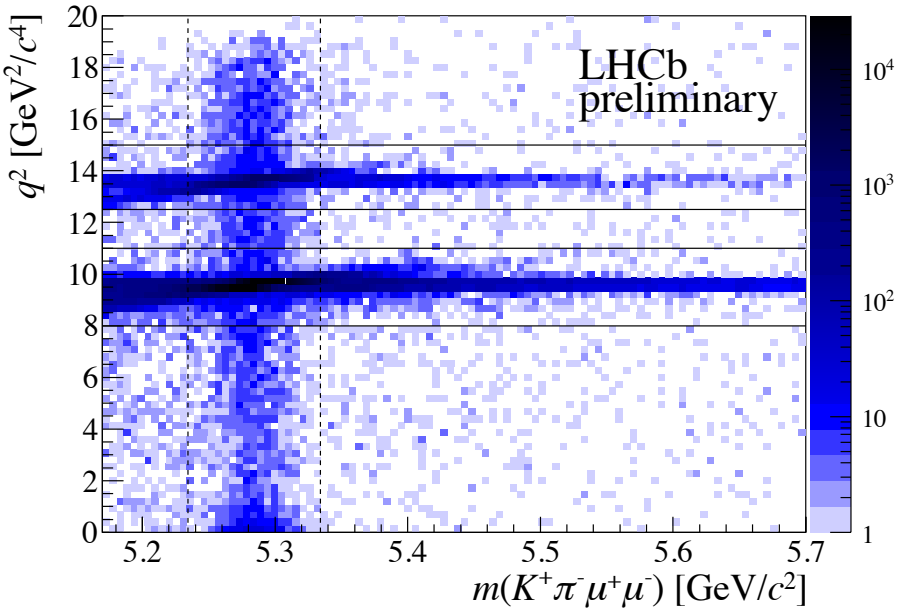

Figure 1: Invariant mass of the $K^+\pi^-\mu^+\mu^-$ system versus q^2. The decay $B^0 \to K^{*0}\mu^+\mu^-$ is clearly visible inside the dashed vertical lines $\pm 50\,\mathrm{MeV}/c^2$ around the fitted B^0 mass. The horizontal lines denote the charmonium regions, where the tree-level decays $B^0 \to J/\psi\, K^{*0}$ and $B^0 \to \psi(2S)K^{*0}$ dominate. These events are excluded from the analysis.

Combinatorial background is further reduced using a boosted decision tree (BDT) [37, 38] which is trained using the data. As a proxy for the signal decay, *sWeighted* [39] $B^0 \to J/\psi(\to \mu^+\mu^-)K^{*0}$ decays are used to train the BDT. Similarly, events from the upper mass sideband $5350 < m(K^+\pi^-\mu^+\mu^-) < 7000\,\mathrm{MeV}/c^2$ are used as a proxy for the background. As input variables, the BDT uses the reconstructed B^0 lifetime and vertex fit quality, the momentum and transverse momentum of the B^0, $\cos\theta_{\mathrm{DIRA}}$, particle identification information from the RICH detectors and the muon system, as well as variables describing the isolation of the final state tracks. To best exploit the data available for training, the k-folding technique [40] is employed. At the chosen working point, the BDT exhibits a background rejection of 97% and a signal efficiency of 85%. Simulation studies indicate that the BDT does not preferentially select certain regions in $m(K^+\pi^-\mu^+\mu^-)$ or $m(K^+\pi^-)$.

The reconstructed $m(K^+\pi^-\mu^+\mu^-)$ mass versus q^2 for candidates which pass the full selection is shown in Fig. 1. The $B^0 \to K^{*0}\mu^+\mu^-$ signal candidates are clearly visible as a vertical band. The contributions from the decays $B^0 \to J/\psi(\to \mu^+\mu^-)K^{*0}$ and $B^0 \to \psi(2S)(\to \mu^+\mu^-)K^{*0}$, which proceed through tree-level $b \to c\bar{c}s$ transitions, can be seen in the two diagonal (nearly horizontal) bands. The decay $B^0 \to J/\psi(\to \mu^+\mu^-)K^{*0}$, is used throughout this analysis as a control channel.

4.1 Backgrounds

Several peaking backgrounds can potentially mimic the signal decay if they are misreconstructed in the detector. Possible pollution from these decays is estimated using samples of simulated events.

The tree-level decays $B^0 \to J/\psi(\to \mu^+\mu^-)K^{*0}$ and the decay $B^0 \to \psi(2S)(\to \mu^+\mu^-)K^{*0}$ dominate in the regions $8.0 < q^2 < 11.0\,\mathrm{GeV}^2/c^4$ and $12.5 < q^2 < 15.0\,\mathrm{GeV}^2/c^4$, respectively, and these q^2 regions are therefore excluded from the analysis of the signal decay. However, these decays can still form a source of background if the μ^- (μ^+) is misidentified as a π^- (K^+) and the π^- (K^+) is misidentified as a μ^- (μ^+). This source of background is removed by requiring that the π^- (K^+) is not also identified as a muon when the mass of the $\pi^-\mu^+$ ($K^+\mu^-$) system is also consistent with that of a J/ψ or $\psi(2S)$. Possible pollution from $B^0 \to K^{*0}\phi(\to \mu^+\mu^-)$ decays is removed by excluding the q^2 region $0.98 < q^2 < 1.10\,\mathrm{GeV}^2/c^4$ from the analysis.

The decay $\Lambda_b^0 \to pK^-\mu^+\mu^-$, which is expected to proceed predominantly via the $\Lambda(1520) \to pK^-$ resonance, can be a source of peaking background if the proton is misidentified as a pion. Such decays are suppressed by rejecting candidates for which the pion candidate is not clearly identified as a pion by the RICH detectors and which have an invariant mass close to the nominal Λ_b^0 mass when they are reconstructed using the proton mass hypothesis for the reconstructed pion candidate. Similarly, possible $\Lambda_b^0 \to pK^-\mu^+\mu^-$ backgrounds with double misidentification of the hadrons, *i.e.* where the proton is misidentified as a kaon and the pion is misidentified as a proton, are suppressed using PID information.

The decay $B_s^0 \to \phi(\to K^+K^-)\mu^+\mu^-$ can mimic the signal decay if one of the kaons is misidentified as a pion. This background is suppressed by requiring stringent PID criteria if the reconstructed invariant masses of the B^0 candidate and K^{*0} are consistent with the nominal B_s^0 and ϕ masses after assigning to the pion the kaon mass.

The decay $B^+ \to K^+\mu^+\mu^-$ can form a background if a low momentum pion from elsewhere in the event is added to form a four particle final state. The resulting invariant mass $m(K^+\pi^-\mu^+\mu^-)$ will be larger than the nominal B^0 mass but can contribute to the upper mass-sideband. Such decays can therefore distort the estimation of the angular distribution of the residual background which is assessed from this sideband. This background is suppressed by removing candidates with $5220 < m(K^+\mu^+\mu^-) < 5340\,\mathrm{MeV}/c^2$. It is also possible to have backgrounds from $B^{0,+} \to K^{*0,+}\mu^+\mu^-$ decays, where the pion from the K^* is replaced by another pion from the rest of the event. This background typically has a reconstructed mass below the nominal B^0 mass and no veto is required. Finally, signal decays where the K^+ is misidentified as the π^+ and the π^- is misidentified as the K^- can be a source of background. These signal-swap decays are suppressed using PID information.

After all vetoes are applied, the largest peaking background contribution is expected to be from $\Lambda_b^0 \to pK^-\mu^+\mu^-$ decays. The residual background from these decays is expected to be at a level of $(1.0 \pm 0.4)\%$ of the signal yield. The next largest backgrounds are $B^0 \to K^{*0}\mu^+\mu^-$ signal swaps at $(0.64 \pm 0.06)\%$, misidentified $B_s^0 \to \phi\mu^+\mu^-$ events at

$(0.33 \pm 0.12)\%$ and $B^0 \to J/\psi\, K^{*0}$ decays with double misidentification at $(0.05 \pm 0.05)\%$ of the signal, respectively. These backgrounds are deemed sufficiently small to be neglected in the angular analysis, but are considered further as sources of systematic uncertainty. The background from $B^{0,+} \to K^{*0,+}\mu^+\mu^-$ decays where a pion (or kaon) is replaced with a pion (kaon) from elsewhere in the event, which do not peak in the signal region, is at a level of $<2\%$ of the signal yield.

5 Angular acceptance

The trigger, reconstruction and selection of the signal decay distort the distributions of the decay angles θ_l, θ_K and ϕ, as well as the q^2 distribution, giving rise to a so-called angular acceptance effect. The dominant acceptance effects come from momentum and impact parameter requirements. In particular, the implicit momentum threshold that is required for tracks to traverse the magnetic spectrometer removes low momentum tracks. In contrast to the previous LHCb analyses [1,7], the acceptance is not assumed to factorise in the three decay angles. Instead, the efficiency is parameterised in four dimensions, according to

$$\varepsilon(\cos\theta_l, \cos\theta_K, \phi, q^2) = \sum_{klmn} c_{klmn} P_k(\cos\theta_l) P_l(\cos\theta_K) P_m(\phi) P_n(q^2), \tag{6}$$

where the terms $P_i(x)$ denote Legendre polynomials of order i. The coefficients c_{klmn} are determined using a principal moment analysis of simulated three-body $B^0 \to K^{*0}\mu^+\mu^-$ phase-space decays. The parameterisation in terms of all of the kinematic variables that describe the decay make this determination independent of the model used for this simulation. For $\cos\theta_l$ ($\cos\theta_K$), polynomials of fifth (sixth) order are used. For the angle ϕ a polynomial of sixth order is used and for q^2, the parameterisation comprises a seventh order polynomial. The angular acceptance in $\cos\theta_\ell$, $\cos\theta_K$ and ϕ is shown for $0.1 < q^2 < 0.98\,\mathrm{GeV}^2/c^4$ and $18.0 < q^2 < 19.0\,\mathrm{GeV}^2/c^4$ in Fig. 2. The acceptance varies smoothly as a function of q^2 between these extremes. The description of the angular acceptance is cross-checked, for $q^2 = m^2(J/\psi)$, using the decay $B^0 \to J/\psi\, K^{*0}$. This decay can be selected in the data with background contamination at the $< 1\%$ level and the angular structure has been determined by measurements made by the BaBar, Belle and LHCb collaborations [41–43]. Applying the acceptance correction derived using the above method, the $B^0 \to J/\psi\, K^{*0}$ angular observables obtained from the LHCb data are in good agreement with these previous measurements. The angular fit of the LHCb data is shown in Fig. 7 of Appendix B.

6 The $K^+\pi^-\mu^+\mu^-$ and $K^+\pi^-$ mass distributions

The $K^+\pi^-\mu^+\mu^-$ invariant mass distribution of the signal candidates is modelled using the sum of two Gaussian functions with common mean, each with a power-law tail on the low-mass side. The parameters describing the signal mass-shape are determined from a fit

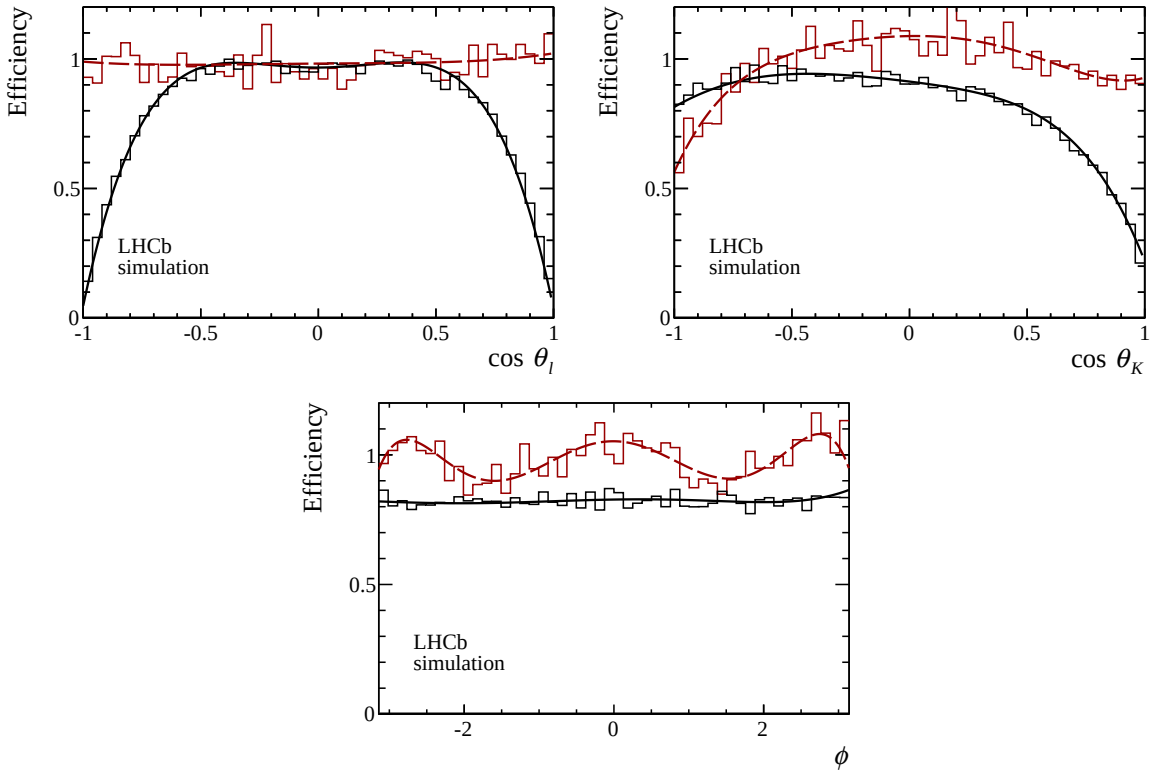

Figure 2: Angular efficiency in $\cos\theta_\ell$, $\cos\theta_K$ and ϕ, as determined from a principal moment analysis of simulated three-body $B^0 \to K^{*0}\mu^+\mu^-$ phase-space decays. The efficiency is shown for the regions $0.1 < q^2 < 0.98\,\mathrm{GeV}^2/c^4$ (black solid line) and $18.0 < q^2 < 19.0\,\mathrm{GeV}^2/c^4$ (red dashed line). The histograms indicate the distribution of simulated three-body $B^0 \to K^{*0}\mu^+\mu^-$ phase-space decays used to determine the acceptance. The absolute normalisation of the dsitributions is arbitrary.

to the $B^0 \to J/\psi\, K^{*0}$ decay in the data, as shown in Fig. 3, and are subsequently fixed when fitting the $B^0 \to K^{*0}\mu^+\mu^-$ candidates. A component is included in the fit to account for $\overline{B}{}^0_s \to J/\psi\, K^{*0}$ decays, which are at a level of 0.8% of the $B^0 \to J/\psi\, K^{*0}$ signal [44]. In samples of simulated events, the mass resolution is observed to vary with q^2. A scale factor is therefore taken from the simulation and is used to correct the width of the Gaussian functions in the different q^2 bins in data. Combinatorial backgrounds are well described by a single falling exponential distribution in $m(K^+\pi^-\mu^+\mu^-)$.

As detailed in Section 7, the $m(K^+\pi^-)$ distribution is also fitted. To describe this distribution, the K^{*0} signal component is modelled using a relativistic Breit-Wigner for the P-wave component and the LASS parameterisation [45] for the S-wave component. The background is described by a linear function in $m(K^+\pi^-)$.

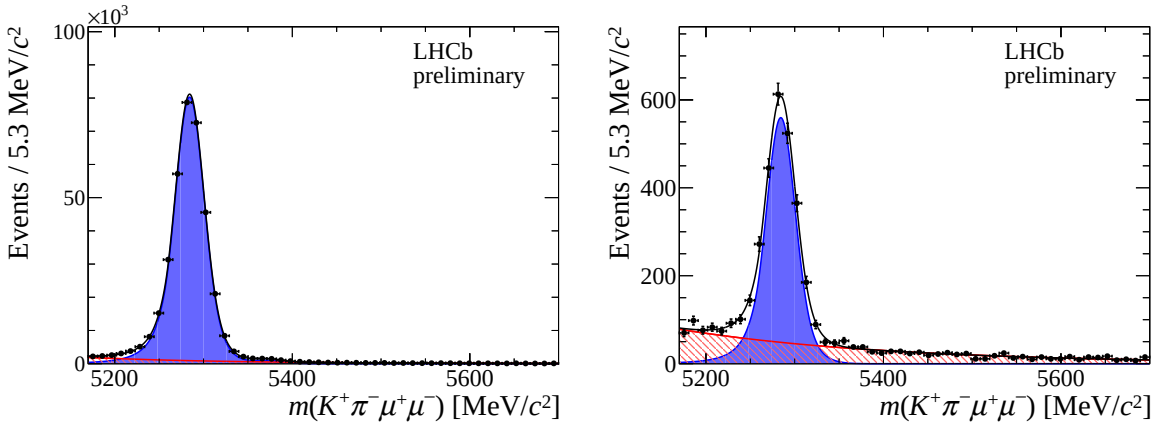

Figure 3: Invariant mass $m(K^+\pi^-\mu^+\mu^-)$ for (left) the control decay $B^0 \to J/\psi K^{*0}$ and (right) the signal decay $B^0 \to K^{*0}\mu^+\mu^-$, integrated over the full q^2 range. The $B^0 \to K^{*0}\mu^+\mu^-$ signal yield integrated over q^2 is determined to be 2398 ± 57. Overlaid are the projections of the total fitted distribution (black line) and its different components. The signal is shown by the blue component and the background is shown by the red hatched component.

7 Angular analysis

In each q^2 bin, an unbinned maximum likelihood fit to $m(K^+\pi^-\mu^+\mu^-)$ and the three decay angles $\cos\theta_l$, $\cos\theta_K$ and ϕ is used to determine the angular observables introduced in Section 2. The $K^+\pi^-\mu^+\mu^-$ invariant mass is included in the fit to separate signal from background. The signal and background mass distributions are parameterised as described in Section 6. The background angular distribution is modelled by a series of Chebychev polynomials in $\cos\theta_\ell$, $\cos\theta_K$ and ϕ up to order two.

In order to correctly describe the signal angular distribution, the angular acceptance described in Section 5 needs to be accounted for. The acceptance is treated in one of two ways depending on the q^2 range being fitted. In narrow q^2 bins, the acceptance can be treated as being constant across each bin. The acceptance is then included in the fit by multiplying Eq. 5 by the acceptance function evaluated at the centre of each bin. In the wider $1.1 < q^2 < 6.0\,\mathrm{GeV}^2/c^4$ and $15.0 < q^2 < 19.0\,\mathrm{GeV}^2/c^4$ bins, the shape of the acceptance can vary significantly across the q^2 bin. To account for the acceptance, the candidates are therefore weighted in the likelihood fit by the inverse of their efficiency. The event weights are corrected such that this pseudo-likelihood fit has confidence intervals with the correct coverage.

In all of the q^2 bins, to ensure correct coverage for the angular observables, the Feldman-Cousins method [46] is used to determine the uncertainties. Nuisance parameters are treated using the plug-in method [47] throughout.

In order to better constrain the S-wave fraction, a simultaneous fit of the $m(K^+\pi^-)$ distribution is also performed using the parameterisation described in Section 6. The signal and background yields are shared between this fit and that made to the angular distribution.

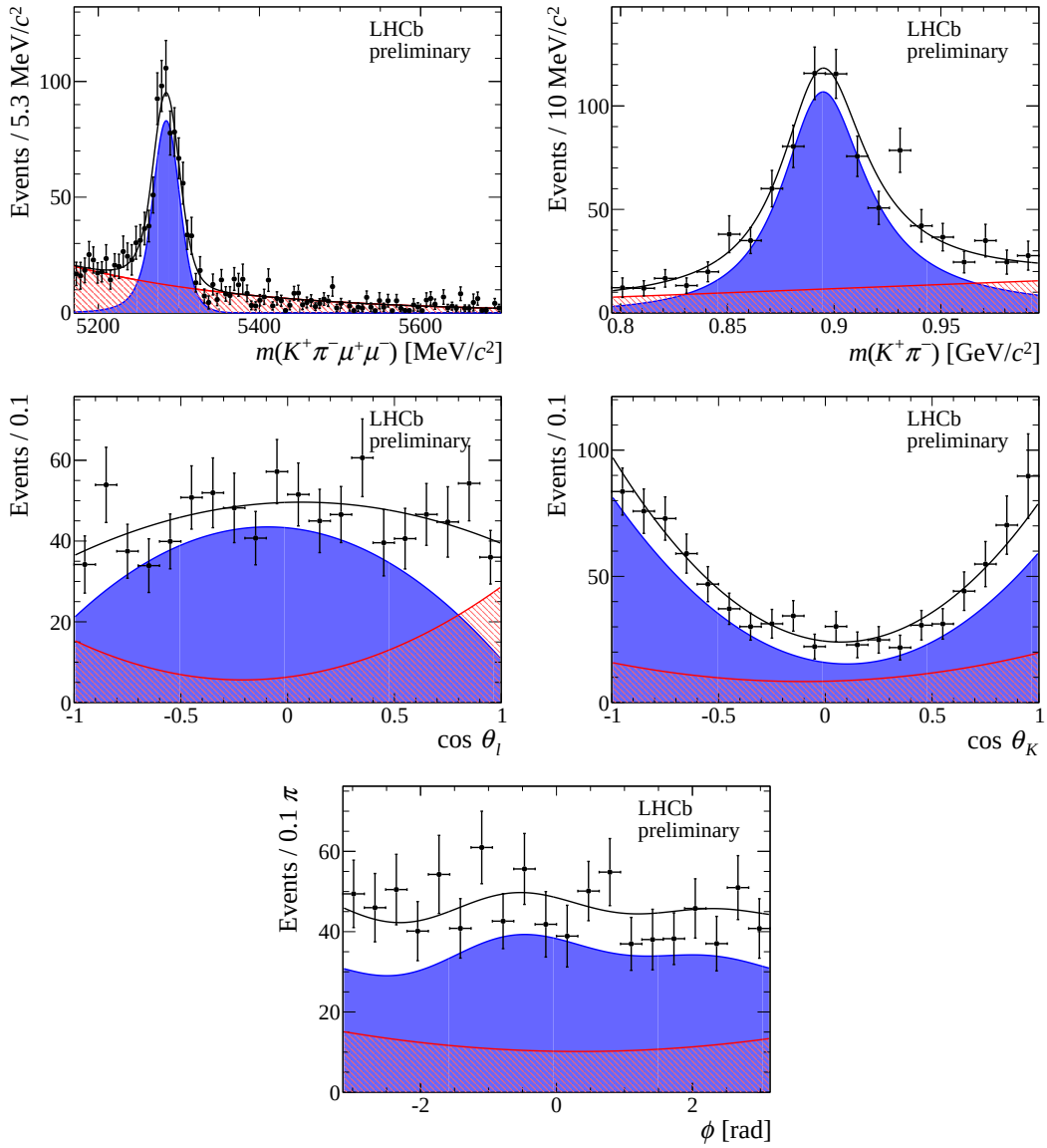

Figure 4: Angular and mass distributions for the q^2 bin $1.1 < q^2 < 6.0\,\mathrm{GeV}^2/c^4$. The $m(K^+\pi^-)$ distribution and the three decay angles are given in the signal mass window $\pm 50\,\mathrm{MeV}/c^2$ around the nominal B^0 mass. Overlaid are the projections of the total fitted distribution (black line) and its different components. The signal is shown by the blue component and the background is shown by the red hatched component.

Fig. 4 shows the projections of the fitted probability density function on the angular and mass distributions for the $1.1 < q^2 < 6.0\,\mathrm{GeV}^2/c^4$ q^2 bin. Good agreement of the fitted function with the data is observed. Projections for the other q^2 bins are provided in Appendix B.

8 Systematic uncertainties

Sources of systematic uncertainty are considered if they could affect the mass or angular distribution of either the signal or background candidates. The size of each systematic uncertainty is estimated using pseudo-experiments in which one or more parameters are varied. The pseudo-experiments are generated with signal yields many times larger than that of the data, in order to eliminate statistical fluctuations. The angular observables are determined from these pseudo-experiments using the nominal model and the systematically varied model. A systematic uncertainty is then assigned based on the typical variation between the two models.

For the signal, the main systematic effects arise from uncertainties that might lead to a biased estimate of the angular acceptance. Four separate sources for such uncertainties are considered: the statistical uncertainty on the acceptance correction resulting from the limited size of the simulation sample from which it is determined; an uncertainty arising from residual data-simulation differences; an uncertainty associated with the parameterisation that is used to describe the acceptance function; and an uncertainty associated with evaluating the acceptance at a fixed point in q^2.

The statistical uncertainty on the acceptance function is evaluated using pseudo-experiments that are generated by coherently fluctuating the acceptance parameters (according to the covariance matrix for the angular moments of the acceptance). To evaluate the uncertainty associated with the particular choice of order for the polynomial that is used to describe the acceptance function, pseudo-experiments are produced in which the polynomial order is increased by two in q^2 and each of the angles.

After correcting the B^0 momentum spectrum, detector occupancy and PID performance of the simulation to match the data, there is very good agreement between simulated and genuine $B^0 \to J/\psi\, K^{*0}$ decays. There are, however, some small remaining differences in the momentum and transverse momentum of the reconstructed pion that can affect the determination of the acceptance correction. A new acceptance correction is derived after re-weighting the phase-space sample to account for the differences observed. A more extreme variation has also been considered in which an acceptance correction is derived without any of the data-simulation corrections applied. The larger of the variations observed is added as a systematic uncertainty.

In fitting the narrow bins of q^2, the acceptance is evaluated using the q^2 value of the bin centre. Pseudo-experiments are performed to assess the bias generated by this choice, by instead using the value of q^2 of the left- or right-hand bin boundary. This variation encompasses the largest possible acceptance variation across the bin.

In principle, it is also possible to bias the angular distribution of the signal if there is a sizeable production, detection or direct CP asymmetry between B^0 and $\overline{B}^0$ mesons. These asymmetries are, however, known to be small [48]. There may also be small contributions from the tails of higher-spin K^* states (decaying to $K^+\pi^-$) in the $795.9 < m(K^+\pi^-) < 995.9\,\mathrm{MeV}/c^2$ window. Simulation studies indicate that any bias arising from these higher-K^* states is negligible compared to the statistical uncertainty on the angular observables.

For the background modelling, two sources of systematic uncertainty are considered. The first of these is associated with the choice of second order polynomials to model the background angular distribution in the fit. It is not possible to fit a more complex model to the data, because of the small number of background candidates. Therefore, to test the model, the BDT cut is relaxed and the background candidates are fitted with a fourth-order polynomial in each of the three angles. Pseudo-experiments are then generated according to this fourth-order model and fitted with the second-order model.

Systematic uncertainties are also assessed for the different sources of peaking background, which are neglected in the angular analysis. As detailed in Section 4.1, the most important backgrounds are those from $B_s^0 \to \phi\mu^+\mu^-$ and $\Lambda_b^0 \to pK^-\mu^+\mu^-$ decays, where a kaon or proton is misidentified as pion; and $B^0 \to K^{*0}\mu^+\mu^-$ decays, where the kaon and pion are both misidentified. Taking the angular distribution of the background from simulated events, pseudo-experiments are generated with these backgrounds included and the angular observables determined as if the background were not present. Pseudo-experiments are also performed in which the angular distribution of the $B_s^0 \to \phi\mu^+\mu^-$ and $\Lambda_b^0 \to pK^-\mu^+\mu^-$ decays are taken from data, by removing PID information from the BDT and inverting the background vetoes.

Finally, systematic uncertainties are also assessed for the signal mass modelling in $m(K^+\pi^-\mu^+\mu^-)$ and $m(K^+\pi^-)$. To assess the model of $m(K^+\pi^-\mu^+\mu^-)$, a fit is performed to $B^0 \to J/\psi\, K^{*0}$ data using the sum of two Gaussians without the power law tails. To assess the modelling of $m(K^+\pi^-)$, pseudo-experiments are produced systematically varying the S- and P-wave line-shape parameters, for example varying the radius used in the relativistic Breit-Wigner. For the S-wave, the LASS line-shape is also exchanged for an Isobar model with $K_0^*(800)$ and $K_0^*(1430)$ contributions.

For $F_{\rm L}$, the largest source of systematic uncertainty comes from the data-simulation comparison of the pion momenta. The systematic uncertainty assigned to this effect is at the level of $0.01 - 0.02$, depending on the q^2 bin. This uncertainty constitutes up to 30% of the statistical uncertainty.

For S_4, the largest source of systematic uncertainty comes from the choice of polynomial order for the angular acceptance. If polynomials two orders higher are used, a variation of ~ 0.01 is observed. This uncertainty is up to 20% of the statistical uncertainty.

For the remaining observables, the uncertainties arising from the data-simulation comparison and the acceptance order are small. However, there are three other significant sources of systematic uncertainty. First, throughout the full q^2 range, peaking backgrounds introduce a systematic uncertainty at the level of $\lesssim 0.01$. Second, in the first two q^2 bins (where the acceptance changes most rapidly), the uncertainty arising from using the bin centre, as opposed to a bin edge, is at the level of $\lesssim 0.01$. Finally, at high q^2, the statistical precision on the acceptance correction leads to a systematic uncertainty at the level of $\lesssim 0.01$.

Combining the various sources of systematic effects, the total systematic uncertainty on $F_{\rm L}$ is typically 30% of the statistical uncertainty. For the other angular observables the uncertainty is typically 10-20% of the statistical uncertainty, depending on q^2 and the observable considered. When added in quadrature, systematic effects therefore remain

small compared to the total uncertainty. The dominant sources of systematic uncertainty can all be reduced in future analyses with larger datasets.

9 Results

The likelihood fits for the different q^2 bins are shown in Figs 8-16. The *CP*-averaged observables $F_{\rm L}$, $A_{\rm FB}$ and S_3 through S_9 that are obtained from these fits, are shown together with the SM theoretical predictions in Fig. 5. The SM predictions are based on the description in Ref. [18]. In contrast to the alternative SM predictions that are available in Refs. [19, 49–54], this prediction updates the form-factor calculations from Ref. [55] to account for the known correlation between the different form-factors [56]. Light-cone sum rule predictions which are valid in the low-q^2 region, are also combined with lattice determinations at high q^2 [57, 58] to yield more precise determinations of the form-factors over the full q^2 range. The predictions are made in the region $0.1 < q^2 < 6.0\,{\rm GeV}^2/c^4$ and $15.0 < q^2 < 19.0\,{\rm GeV}^2/c^4$. No predictions are included for the region close to the narrow $c\overline{c}$ resonances, the J/ψ and $\psi(2S)$, where many of the assumptions that go into the SM predictions are thought to break down.

The measurements are tabulated in Table 3 with the statistical and systematic uncertainties separated. The correlation matrices between the observables are also given in Appendix C. In general, the correlations are small. The exception to this is the correlation of $A_{\rm FB}$ and $F_{\rm L}$, which can be as large as $\sim 50\%$. This correlation arises from the requirement that Eq. 4 be positive in the entire phase-space. The values of $F_{\rm S}$ obtained from the fits are consistent with the $\sim 5\%$ S-wave pollution observed in $B^0 \to J/\psi\, K^{*0}$ data [41–43].

To understand the compatibility of the measurements with the SM, the correlations between the observables must be taken into account. Such an analysis is beyond the scope of this note. Neglecting the correlations, the results appear largely in agreement with the SM predictions, with the exception of the observable S_5. A mild tension can also be seen in the measured $A_{\rm FB}$ distribution.

The tension in S_5 can also be seen in the related distribution of $P_5' = S_5/\sqrt{F_{\rm L}(1-F_{\rm L})}$ in Fig. 6. This observable is determined by reparameterising the angular distribution accordingly. For the P_5' observable, a prediction from Ref. [13] is shown. This prediction is computed in the region $0.1 < q^2 < 8.0\,{\rm GeV}^2/c^4$, where a local tension with the SM prediction was seen in the $1\,{\rm fb}^{-1}$ LHCb analysis [7].[2] In this analysis, a tension with the SM prediction (from Ref. [13]) at a level of 2.9σ is observed in each of the $4.0 < q^2 < 6.0\,{\rm GeV}^2/c^4$ and $6.0 < q^2 < 8.0\,{\rm GeV}^2/c^4$ bins. A naïve combination of these deviations, based on a χ^2 probability with two degrees of freedom and assuming the SM predictions in the two bins are uncorrelated, yields a local tension of 3.7σ.

Although completely consistent with the SM predictions, the $A_{\rm FB}$ fit results are systematically $\lesssim 1\sigma$ below the SM prediction in the region with $1.1 < q^2 < 6.0\,{\rm GeV}^2/c^4$. The zero-crossing point of $A_{\rm FB}$, q_0^2, has been determined to be $(3.7^{+0.8}_{-1.1})\,{\rm GeV}^2/c^4$ using

[2] The prediction in Ref. [13] is an update of the SM calculation used for comparison in the $1\,{\rm fb}^{-1}$ LHCb analysis [7].

the method described in Ref. [1]. The uncertainty on q_0^2 is purely statistical and is determined by a bootstrapping technique. The value of q_0^2 is in good agreement with SM predictions which are typically around $4.0\,\mathrm{GeV}^2/c^4$, with a relative uncertainty smaller than 10% [59, 60]. The experimental uncertainty on q_0^2 is comparable to that given in Ref. [1], despite the larger dataset used in the present analysis, owing to the shallower gradient of A_{FB} in the region of the zero-crossing point.

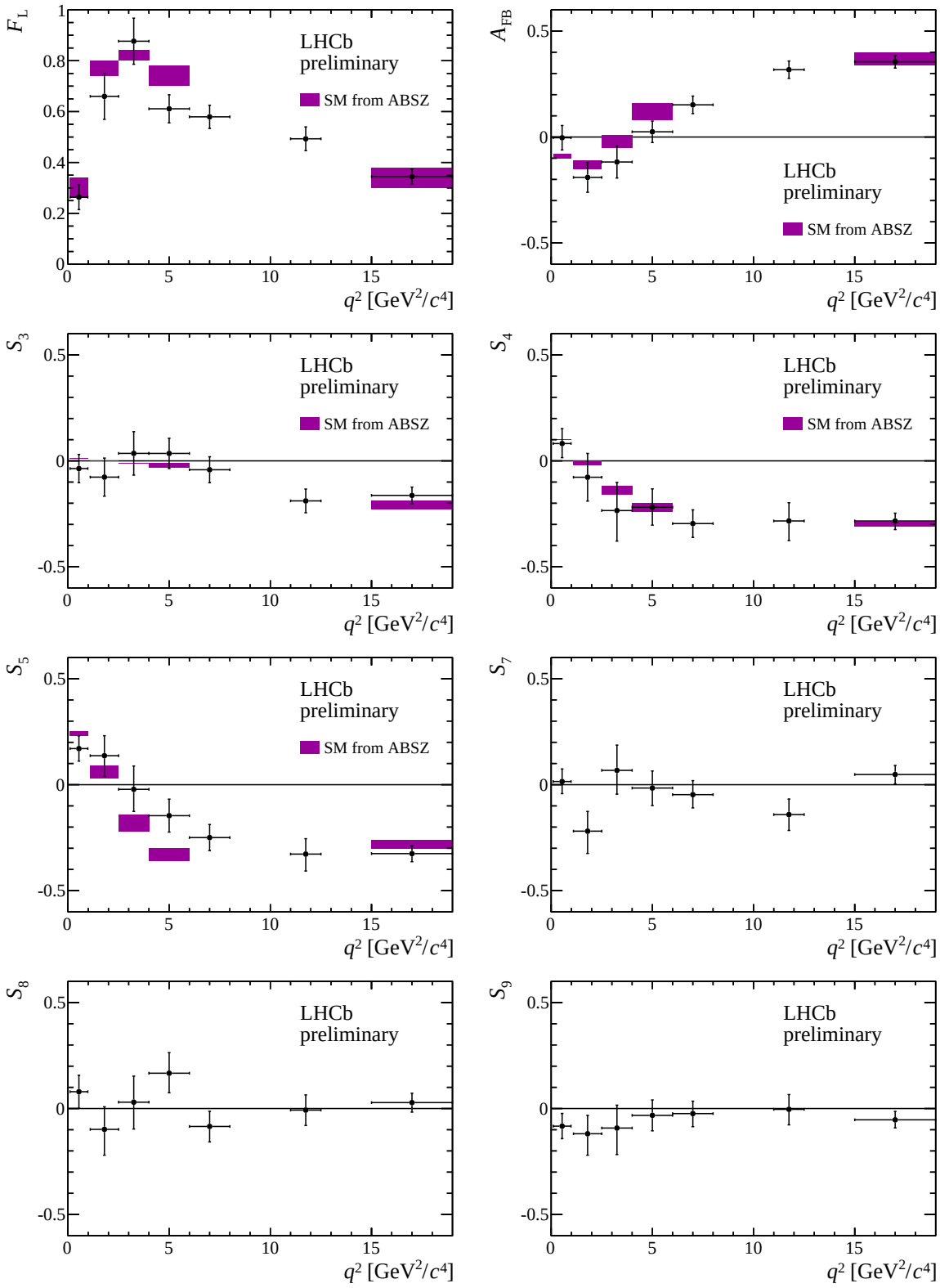

Figure 5: The *CP*-averaged observables in bins of q^2. The shaded boxes show the SM prediction taken from Ref. [61].

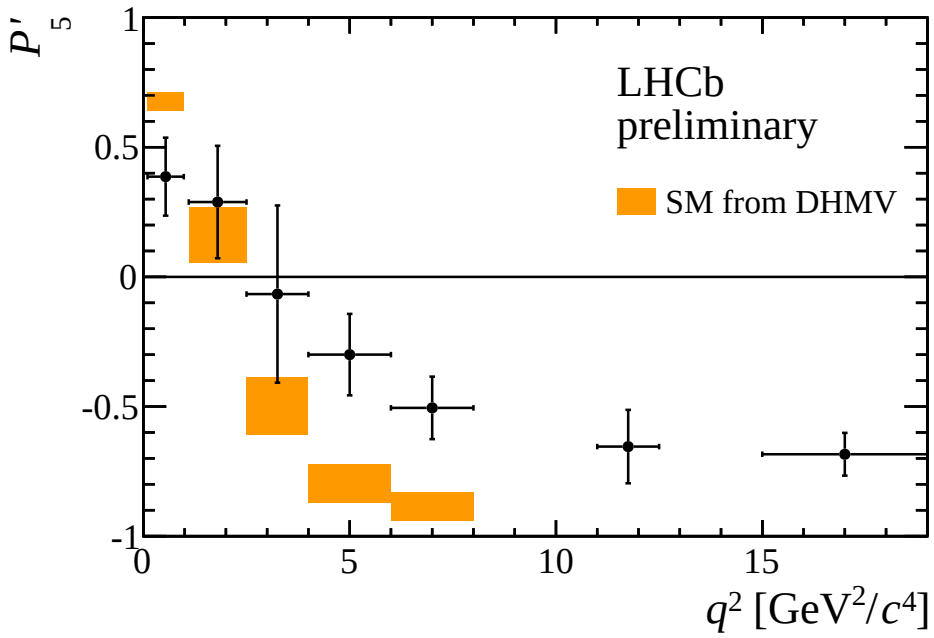

Figure 6: The observable P'_5 in bins of q^2. The shaded boxes show the SM prediction taken from Ref. [13].

10 Conclusions

This note describes an updated angular analysis of the $B^0 \to K^{*0}\mu^+\mu^-$ decay, using the full LHCb Run I data sample, corresponding to an integrated luminosity of $3\,\text{fb}^{-1}$. The data were taken at centre-of-mass energies of 7 and 8 TeV during 2011 and 2012, respectively. Using the full angular distribution, the *CP*-averaged observables, F_L, A_FB and S_3 through S_9, are measured. This analysis is the first to determine a complete set of *CP*-averaged observables. Neglecting the correlations between these observables, the results are largely in agreement with the SM predictions. However, the observable S_5 is in poor agreement with the SM prediction in the region $4.0 < q^2 < 8.0\,\text{GeV}^2/c^4$. This discrepancy was previously seen in measurements of the related observable P_5', which were made with the 2011 LHCb dataset. With the addition of the 2012 data, the P_5' measurements are only compatible with the SM prediction at a level of 3.7σ in $4.0 < q^2 < 8.0\,\text{GeV}^2/c^4$. To better understand the compatibility of the data with the SM a global analysis of the data, taking into account the correlation between the observables, is necessary. A mild tension can also be seen in the A_FB distribution, where the measurements are systematically $\lesssim 1\sigma$ below the SM prediction in the region $1.1 < q^2 < 6.0\,\text{GeV}^2/c^4$. The zero-crossing point of A_FB has been determined to be $(3.7^{+0.8}_{-1.1})\,\text{GeV}^2/c^4$, which is in good agreement with the SM prediction.

References

[1] LHCb collaboration, R. Aaij *et al.*, *Differential branching fraction and angular analysis of the decay $B^0 \to K^{*0}\mu^+\mu^-$*, JHEP **08** (2013) 131, arXiv:1304.6325.

[2] BaBar collaboration, B. Aubert *et al.*, *Measurements of branching fractions, rate asymmetries, and angular distributions in the rare decays $B \to K\ell^+\ell^-$ and $B \to K^*\ell^+\ell^-$*, Phys. Rev. **D73** (2006) 092001, arXiv:hep-ex/0604007.

[3] Belle collaboration, J.-T. Wei *et al.*, *Measurement of the differential branching fraction and forward-backward asymmetry for $B \to K^{(*)}\ell^+\ell^-$*, Phys. Rev. Lett. **103** (2009) 171801, arXiv:0904.0770.

[4] CDF collaboration, T. Aaltonen *et al.*, *Measurements of the angular distributions in the Decays $B \to K^{(*)}\mu^+\mu^-$ at CDF*, Phys. Rev. Lett. **108** (2012) 081807, arXiv:1108.0695.

[5] ATLAS collaboration, *Angular analysis of $B_d \to K^{*0}\mu^+\mu^-$ with the ATLAS experiment*, ATLAS-CONF-2013-038, 2013.

[6] CMS collaboration, S. Chatrchyan *et al.*, *Angular analysis and branching fraction measurement of the decay $B^0 \to K^{*0}\mu^+\mu^-$*, Phys. Lett. **B727** (2013) 77, arXiv:1308.3409.

[7] LHCb collaboration, R. Aaij *et al.*, *Measurement of form-factor-independent observables in the decay $B^0 \to K^{*0}\mu^+\mu^-$*, Phys. Rev. Lett. **111** (2013) 191801, arXiv:1308.1707.

[8] S. Descotes-Genon, J. Matias, and J. Virto, *Understanding the $B \to K^*\mu^+\mu^-$ Anomaly*, Phys. Rev. **D88** (2013) 074002, arXiv:1307.5683.

[9] W. Altmannshofer and D. M. Straub, *New physics in $B \to K^*\mu\mu$?*, Eur. Phys. J. **C73** (2013) 2646, arXiv:1308.1501.

[10] F. Beaujean, C. Bobeth, and D. van Dyk, *Comprehensive Bayesian analysis of rare (semi)leptonic and radiative B decays*, Eur. Phys. J. **C74** (2014) 2897, arXiv:1310.2478.

[11] T. Hurth and F. Mahmoudi, *On the LHCb anomaly in $B \to K^*\ell^+\ell^-$*, JHEP **04** (2014) 097, arXiv:1312.5267.

[12] S. Jäger and J. Martin Camalich, *On $B \to Vll$ at small dilepton invariant mass, power corrections, and new physics*, JHEP **05** (2013) 043, arXiv:1212.2263.

[13] S. Descotes-Genon, L. Hofer, J. Matias, and J. Virto, *On the impact of power corrections in the prediction of $B \to K^*\mu^+\mu^-$ observables*, JHEP **1412** (2014) 125, arXiv:1407.8526.

[14] J. Lyon and R. Zwicky, *Resonances gone topsy turvy - the charm of QCD or new physics in $b \to s\ell^+\ell^-$?*, arXiv:1406.0566.

[15] W. Altmannshofer, S. Gori, M. Pospelov, and I. Yavin, *Quark flavor transitions in $L_\mu - L_\tau$ models*, Phys. Rev. **D89** (2014) 095033, arXiv:1403.1269.

[16] A. Crivellin, G. D'Ambrosio, and J. Heeck, *Explaining $h \to \mu^\pm\tau^\mp$, $B \to K^*\mu^+\mu^-$ and $B \to K\mu^+\mu^-/B \to Ke^+e^-$ in a two-Higgs-doublet model with gauged $L_\mu - L_\tau$*, arXiv:1501.00993.

[17] R. Gauld, F. Goertz, and U. Haisch, *An explicit Z'-boson explanation of the $B \to K^*\mu^+\mu^-$ anomaly*, JHEP **01** (2014) 069, arXiv:1310.1082.

[18] W. Altmannshofer and D. M. Straub, *State of new physics in $b \to s$ transitions*, arXiv:1411.3161.

[19] F. Mahmoudi, S. Neshatpour, and J. Virto, *$B \to K^*\mu^+\mu^-$ optimised observables in the MSSM*, Eur. Phys. J. **C74** (2014) 2927, arXiv:1401.2145.

[20] A. Datta, M. Duraisamy, and D. Ghosh, *Explaining the $B \to K^*\mu^+\mu^-$ data with scalar interactions*, Phys. Rev. **D89** (2014) 071501, arXiv:1310.1937.

[21] W. Altmannshofer *et al.*, *Symmetries and Asymmetries of $B \to K^*\mu^+\mu^-$ Decays in the Standard Model and Beyond*, JHEP **01** (2009) 019, arXiv:0811.1214.

[22] F. Kruger and J. Matias, *Probing new physics via the transverse amplitudes of $\bar{B}^0 \to \bar{K}^*(\to K^-\pi^+)\ell^+\ell^-$ at large recoil*, Phys. Rev. **D71** (2005) 094009, arXiv:hep-ph/0502060.

[23] S. Descotes-Genon, J. Matias, M. Ramon, and J. Virto, *Implications from clean observables for the binned analysis of $B \to K^*\mu^+\mu^-$ at large recoil*, JHEP **01** (2013) 048, arXiv:1207.2753.

[24] LHCb collaboration, A. A. Alves Jr. *et al.*, *The LHCb detector at the LHC*, JINST **3** (2008) S08005.

[25] LHCb collaboration, R. Aaij *et al.*, *LHCb detector performance*, Int. J. Mod. Phys. **A30** (2015) 1530022, arXiv:1412.6352.

[26] R. Aaij *et al.*, *Performance of the LHCb Vertex Locator*, JINST **9** (2014) P09007, arXiv:1405.7808.

[27] R. Arink *et al.*, *Performance of the LHCb Outer Tracker*, JINST **9** (2014) P01002, arXiv:1311.3893.

[28] M. Adinolfi *et al.*, *Performance of the LHCb RICH detector at the LHC*, Eur. Phys. J. **C73** (2013) 2431, arXiv:1211.6759.

[29] A. A. Alves Jr. *et al.*, *Performance of the LHCb muon system*, JINST **8** (2013) P02022, arXiv:1211.1346.

[30] R. Aaij *et al.*, *The LHCb trigger and its performance in 2011*, JINST **8** (2013) P04022, arXiv:1211.3055.

[31] T. Sjöstrand, S. Mrenna, and P. Skands, *PYTHIA 6.4 physics and manual*, JHEP **05** (2006) 026, arXiv:hep-ph/0603175; T. Sjöstrand, S. Mrenna, and P. Skands, *A brief introduction to PYTHIA 8.1*, Comput. Phys. Commun. **178** (2008) 852, arXiv:0710.3820.

[32] I. Belyaev *et al.*, *Handling of the generation of primary events in Gauss, the LHCb simulation framework*, J. Phys. Conf. Ser. **331** (2011) 032047.

[33] D. J. Lange, *The EvtGen particle decay simulation package*, Nucl. Instrum. Meth. **A462** (2001) 152.

[34] P. Golonka and Z. Was, *PHOTOS Monte Carlo: A precision tool for QED corrections in Z and W decays*, Eur. Phys. J. **C45** (2006) 97, arXiv:hep-ph/0506026.

[35] Geant4 collaboration, J. Allison *et al.*, *Geant4 developments and applications*, IEEE Trans. Nucl. Sci. **53** (2006) 270; Geant4 collaboration, S. Agostinelli *et al.*, *Geant4: a simulation toolkit*, Nucl. Instrum. Meth. **A506** (2003) 250.

[36] M. Clemencic *et al.*, *The LHCb simulation application, Gauss: Design, evolution and experience*, J. Phys. Conf. Ser. **331** (2011) 032023.

[37] L. Breiman, J. H. Friedman, R. A. Olshen, and C. J. Stone, *Classification and regression trees*, Wadsworth international group, Belmont, California, USA, 1984.

[38] R. E. Schapire and Y. Freund, *A decision-theoretic generalization of on-line learning and an application to boosting*, Jour. Comp. and Syst. Sc. **55** (1997) 119.

[39] M. Pivk and F. R. Le Diberder, *sPlot: A statistical tool to unfold data distributions*, Nucl. Instrum. Meth. **A555** (2005) 356, arXiv:physics/0402083.

[40] A. Blum, A. Kalai, and J. Langford, *Beating the hold-out: Bounds for k-fold and progressive cross-validation*, in *Proceedings of the Twelfth Annual Conference on Computational Learning Theory*, COLT '99, (New York, NY, USA), pp. 203–208, ACM, 1999. doi: 10.1145/307400.307439.

[41] BaBar Collaboration, B. Aubert *et al.*, *Measurement of decay amplitudes of $B \to J/\psi K^*, \psi(2S)K^*$, and $\chi_{c1}K^*$ with an angular analysis*, Phys. Rev. **D76** (2007) 031102, arXiv:0704.0522.

[42] Belle collaboration, K. Chilikin *et al.*, *Observation of a new charged charmonium like state in $\bar{B}^0 \to J/\psi K^- \pi^+$ decays*, Phys. Rev. **D90** (2014) 112009, arXiv:1408.6457.

[43] LHCb collaboration, R. Aaij *et al.*, *Measurement of the polarization amplitudes in $B^0 \to J/\psi K^*(892)^0$ decays*, Phys. Rev. **D88** (2013) 052002, arXiv:1307.2782.

[44] LHCb collaboration, R. Aaij *et al.*, *Measurement of the $B_s^0 \to J/\psi \bar{K}^{*0}$ branching fraction and angular amplitudes*, Phys. Rev. **D86** (2012) 071102(R), arXiv:1208.0738.

[45] D. Aston *et al.*, *A study of $K^-\pi^+$ scattering in the reaction $K^-p \to K^-\pi^+n$ at 11 GeV/c*, Nuclear Physics B **296** (1988) 493 .

[46] G. J. Feldman and R. D. Cousins, *Unified approach to the classical statistical analysis of small signals*, Phys. Rev. D **57** (1998) 3873, arXiv:physics/9711021.

[47] B. Sen, M. Walker, and M. Woodroofe, *On the unified method with nuisance parameters*, Statistica Sinica **19** (2009) 301.

[48] LHCb collaboration, R. Aaij *et al.*, *Measurement of CP asymmetries in the decays $B^0 \to K^{*0}\mu^+\mu^-$ and $B^+ \to K^+\mu^+\mu^-$*, JHEP **09** (2014) 177, arXiv:1408.0978.

[49] C. Bobeth, G. Hiller, and D. van Dyk, *The Benefits of $\bar{B} \to \bar{K}^* l^+ l^-$ decays at low recoil*, JHEP **07** (2010) 098, arXiv:1006.5013.

[50] S. Jäger and J. Martin Camalich, *Reassessing the discovery potential of the $B \to K^*\ell^+\ell^-$ decays in the large-recoil region: SM challenges and BSM opportunities*, arXiv:1412.3183.

[51] D. Das and R. Sinha, *New physics effects and hadronic form factor uncertainties in $B \to K^*\ell^+\ell^-$*, Phys. Rev. **D86** (2012) 056006, arXiv:1205.1438.

[52] R. R. Horgan, Z. Liu, S. Meinel, and M. Wingate, *Calculation of $B^0 \to K^{*0}\mu^+\mu^-$ and $B_s^0 \to \phi\mu^+\mu^-$ observables using form factors from lattice QCD*, Phys. Rev. Lett. **112** (2014) 212003, arXiv:1310.3887.

[53] C. Hambrock, G. Hiller, S. Schacht, and R. Zwicky, *$B \to K^\star$ form factors from flavor data to QCD and back*, Phys. Rev. **D89** (2014) 074014, arXiv:1308.4379.

[54] T. Hurth, F. Mahmoudi, and S. Neshatpour, *Global fits to $b \to s\ell\ell$ data and signs for lepton non-universality*, JHEP **12** (2014) 053, arXiv:1410.4545.

[55] P. Ball and R. Zwicky, *$B_{(d,s)} \to \rho, \omega, K^*, \phi$ decay form-factors from light-cone sum rules revisited*, Phys. Rev. **D71** (2005) 014029, arXiv:hep-ph/0412079.

[56] A. B. D. M. Straub and R. Zwicky, *$B \to V\ell^+\ell^-$ in the Standard Mode from Light-Cone Sum Rules*, arXiv:1503.05534.

[57] R. R. Horgan, Z. Liu, S. Meinel, and M. Wingate, *Lattice QCD calculation of form factors describing the rare decays $B \to K^*\ell^+\ell^-$ and $B_s \to \phi\ell^+\ell^-$*, Phys. Rev. **D89** (2014) 094501, arXiv:1310.3722.

[58] R. R. Horgan, Z. Liu, S. Meinel, and M. Wingate, *Rare B decays using lattice QCD form factors*, arXiv:1501.00367.

[59] C. Bobeth, G. Hiller, D. van Dyk, and C. Wacker, *The decay $B \to K l^+ l^-$ at low hadronic recoil and model-independent $\Delta B = 1$ constraints*, JHEP **01** (2012) 107, arXiv:1111.2558.

[60] M. Beneke, T. Feldmann, and D. Seidel, *Exclusive radiative and electroweak $b \to d$ and $b \to s$ penguin decays at NLO*, Eur. Phys. J. **C41** (2005) 173, arXiv:hep-ph/0412400.

[61] A. Bharucha, D. Straub, and R. Zwicky, *$B \to V \ell^+ \ell^-$ in the Standard Model from Light-Cone Sum Rules*, to appear.

Appendices

A Results

The results of the likelihood fits described in Section 7 are given in Tables 2 and 3 below.

Table 2: *CP*-averaged angular observables evaluated by the unbinned maximum likelihood fit, in the range $1.1 < q^2 < 6.0\,\mathrm{GeV}^2/c^4$ and $15.0 < q^2 < 19.0\,\mathrm{GeV}^2/c^4$. The first uncertainty is statistical and the second systematic in nature.

	$1.1 < q^2 < 6.0$	$15.0 < q^2 < 19.0$
F_{L}	$0.690\,^{+0.037}_{-0.037} \pm 0.017$	$0.344\,^{+0.029}_{-0.030} \pm 0.008$
A_{FB}	$-0.075\,^{+0.035}_{-0.033} \pm 0.007$	$0.355\,^{+0.028}_{-0.027} \pm 0.009$
S_3	$0.012\,^{+0.038}_{-0.037} \pm 0.004$	$-0.163\,^{+0.035}_{-0.033} \pm 0.009$
S_4	$-0.155\,^{+0.058}_{-0.056} \pm 0.004$	$-0.284\,^{+0.037}_{-0.040} \pm 0.007$
S_5	$-0.023\,^{+0.049}_{-0.052} \pm 0.005$	$-0.325\,^{+0.037}_{-0.038} \pm 0.009$
S_7	$-0.077\,^{+0.052}_{-0.050} \pm 0.006$	$0.048\,^{+0.043}_{-0.044} \pm 0.006$
S_8	$0.028\,^{+0.058}_{-0.055} \pm 0.008$	$0.028\,^{+0.044}_{-0.045} \pm 0.003$
S_9	$-0.064\,^{+0.042}_{-0.041} \pm 0.004$	$-0.053\,^{+0.040}_{-0.038} \pm 0.002$
P'_5	$-0.049\,^{+0.109}_{-0.103} \pm 0.014$	$-0.684\,^{+0.080}_{-0.083} \pm 0.020$

Table 3: *CP*-averaged angular observables evaluated by the unbinned maximum likelihood fit, in the range $q^2_{\rm min} < q^2 < q^2_{\rm max}$ in GeV^2/c^4. The first uncertainty is statistical and the second systematic in nature.

	$0.1 < q^2 < 0.98$	$1.1 < q^2 < 2.5$	$2.5 < q^2 < 4.0$
$F_{\rm L}$	$0.263\,^{+0.046}_{-0.044} \pm 0.017$	$0.660\,^{+0.088}_{-0.075} \pm 0.022$	$0.877\,^{+0.089}_{-0.096} \pm 0.017$
$A_{\rm FB}$	$-0.003\,^{+0.057}_{-0.059} \pm 0.008$	$-0.191\,^{+0.069}_{-0.078} \pm 0.012$	$-0.118\,^{+0.075}_{-0.088} \pm 0.007$
S_3	$-0.036\,^{+0.063}_{-0.062} \pm 0.005$	$-0.077\,^{+0.089}_{-0.104} \pm 0.005$	$0.035\,^{+0.101}_{-0.086} \pm 0.006$
S_4	$0.082\,^{+0.070}_{-0.066} \pm 0.009$	$-0.077\,^{+0.112}_{-0.112} \pm 0.005$	$-0.234\,^{+0.132}_{-0.144} \pm 0.006$
S_5	$0.170\,^{+0.060}_{-0.059} \pm 0.018$	$0.137\,^{+0.094}_{-0.098} \pm 0.009$	$-0.022\,^{+0.110}_{-0.104} \pm 0.008$
S_7	$0.015\,^{+0.059}_{-0.057} \pm 0.006$	$-0.219\,^{+0.093}_{-0.105} \pm 0.003$	$0.068\,^{+0.119}_{-0.112} \pm 0.005$
S_8	$0.079\,^{+0.077}_{-0.078} \pm 0.007$	$-0.098\,^{+0.107}_{-0.122} \pm 0.005$	$0.030\,^{+0.123}_{-0.127} \pm 0.006$
S_9	$-0.083\,^{+0.060}_{-0.059} \pm 0.004$	$-0.119\,^{+0.087}_{-0.101} \pm 0.005$	$-0.092\,^{+0.108}_{-0.125} \pm 0.007$
P'_5	$0.387\,^{+0.141}_{-0.131} \pm 0.052$	$0.289\,^{+0.216}_{-0.200} \pm 0.023$	$-0.066\,^{+0.341}_{-0.360} \pm 0.023$

	$4.0 < q^2 < 6.0$	$6.0 < q^2 < 8.0$	$11.0 < q^2 < 12.5$
$F_{\rm L}$	$0.611\,^{+0.052}_{-0.054} \pm 0.017$	$0.579\,^{+0.043}_{-0.047} \pm 0.015$	$0.493\,^{+0.045}_{-0.051} \pm 0.013$
$A_{\rm FB}$	$0.025\,^{+0.050}_{-0.050} \pm 0.004$	$0.152\,^{+0.040}_{-0.040} \pm 0.008$	$0.318\,^{+0.040}_{-0.040} \pm 0.009$
S_3	$0.035\,^{+0.069}_{-0.067} \pm 0.006$	$-0.042\,^{+0.057}_{-0.058} \pm 0.011$	$-0.189\,^{+0.053}_{-0.031} \pm 0.005$
S_4	$-0.219\,^{+0.086}_{-0.084} \pm 0.008$	$-0.296\,^{+0.065}_{-0.065} \pm 0.011$	$-0.283\,^{+0.086}_{-0.092} \pm 0.009$
S_5	$-0.146\,^{+0.078}_{-0.077} \pm 0.011$	$-0.249\,^{+0.062}_{-0.061} \pm 0.012$	$-0.327\,^{+0.073}_{-0.080} \pm 0.009$
S_7	$-0.016\,^{+0.080}_{-0.083} \pm 0.004$	$-0.047\,^{+0.066}_{-0.062} \pm 0.003$	$-0.141\,^{+0.073}_{-0.075} \pm 0.005$
S_8	$0.167\,^{+0.097}_{-0.092} \pm 0.004$	$-0.085\,^{+0.072}_{-0.073} \pm 0.006$	$-0.007\,^{+0.072}_{-0.073} \pm 0.005$
S_9	$-0.032\,^{+0.073}_{-0.073} \pm 0.004$	$-0.024\,^{+0.059}_{-0.062} \pm 0.005$	$-0.004\,^{+0.070}_{-0.073} \pm 0.006$
P'_5	$-0.300\,^{+0.155}_{-0.156} \pm 0.023$	$-0.505\,^{+0.118}_{-0.117} \pm 0.024$	$-0.654\,^{+0.141}_{-0.153} \pm 0.015$

	$15.0 < q^2 < 17.0$	$17.0 < q^2 < 19.0$
$F_{\rm L}$	$0.349\,^{+0.040}_{-0.039} \pm 0.009$	$0.354\,^{+0.048}_{-0.048} \pm 0.025$
$A_{\rm FB}$	$0.411\,^{+0.040}_{-0.035} \pm 0.008$	$0.305\,^{+0.048}_{-0.046} \pm 0.013$
S_3	$-0.142\,^{+0.046}_{-0.047} \pm 0.007$	$-0.188\,^{+0.076}_{-0.086} \pm 0.017$
S_4	$-0.321\,^{+0.053}_{-0.078} \pm 0.007$	$-0.266\,^{+0.065}_{-0.071} \pm 0.010$
S_5	$-0.316\,^{+0.051}_{-0.058} \pm 0.009$	$-0.323\,^{+0.062}_{-0.069} \pm 0.009$
S_7	$0.061\,^{+0.058}_{-0.060} \pm 0.005$	$0.044\,^{+0.072}_{-0.073} \pm 0.013$
S_8	$0.003\,^{+0.060}_{-0.060} \pm 0.003$	$0.013\,^{+0.067}_{-0.071} \pm 0.005$
S_9	$-0.019\,^{+0.055}_{-0.057} \pm 0.004$	$-0.094\,^{+0.067}_{-0.069} \pm 0.004$
P'_5	$-0.662\,^{+0.112}_{-0.126} \pm 0.017$	$-0.675\,^{+0.138}_{-0.152} \pm 0.017$

B Fit projections

Figure 7 shows the projection of the fitted probability density function on the angular and mass distributions for the $B^0 \to J/\psi K^{*0}$ data. Similarly, Figs 8-16 show the projections for the $B^0 \to K^{*0}\mu^+\mu^-$ data in the different q^2 bins.

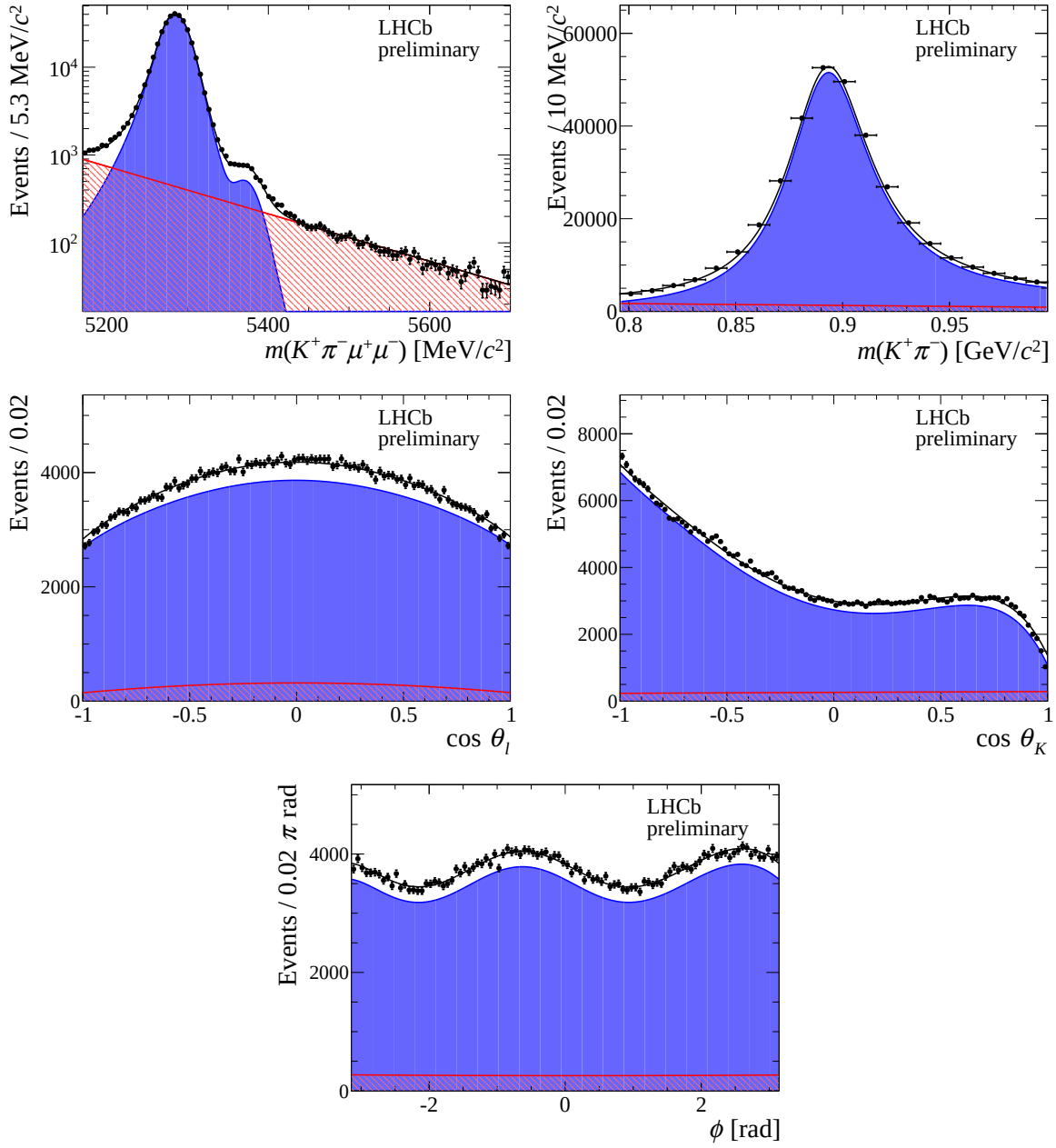

Figure 7: Angular and mass distribution of $B^0 \to J/\psi K^{*0}$ candidates in data. A small signal component is also included in the fit to account for $\overline{B}{}^0_s \to J/\psi K^{*0}$ decays. Overlaid are the projections of the total fitted distribution (black line) and its different components. The signal is shown by the blue component and the background is shown by the red hatched component.

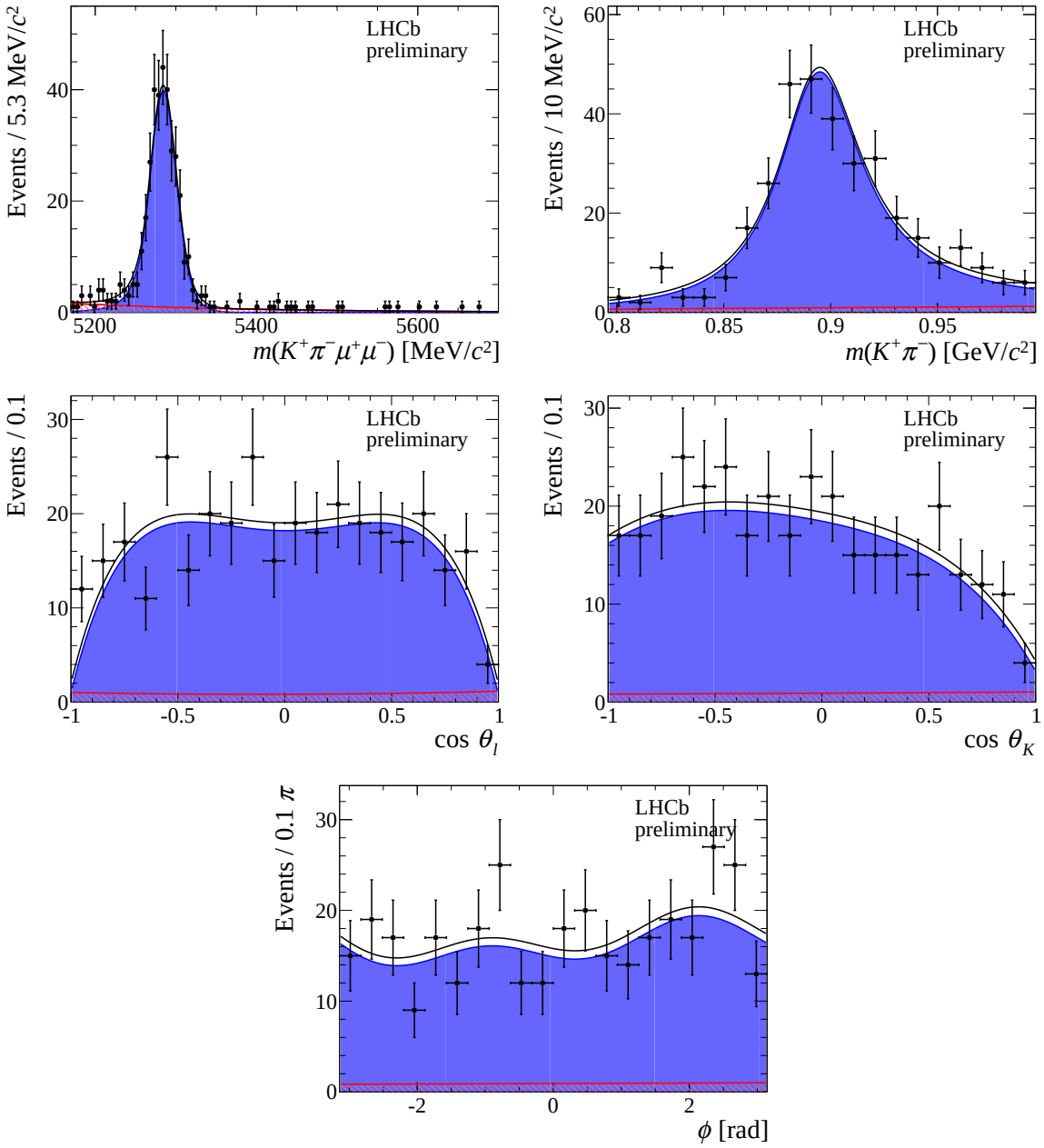

Figure 8: Angular and mass distributions for the q^2 bin $0.1 < q^2 < 0.98\,\mathrm{GeV}^2/c^4$. The $m(K^+\pi^-)$ distribution and the three decay angles are given in the signal mass window $\pm 50\,\mathrm{MeV}/c^2$ around the nominal B^0 mass. Overlaid are the projections of the total fitted distribution (black line) and its different components. The signal is shown by the blue component and the background is shown by the red hatched component.

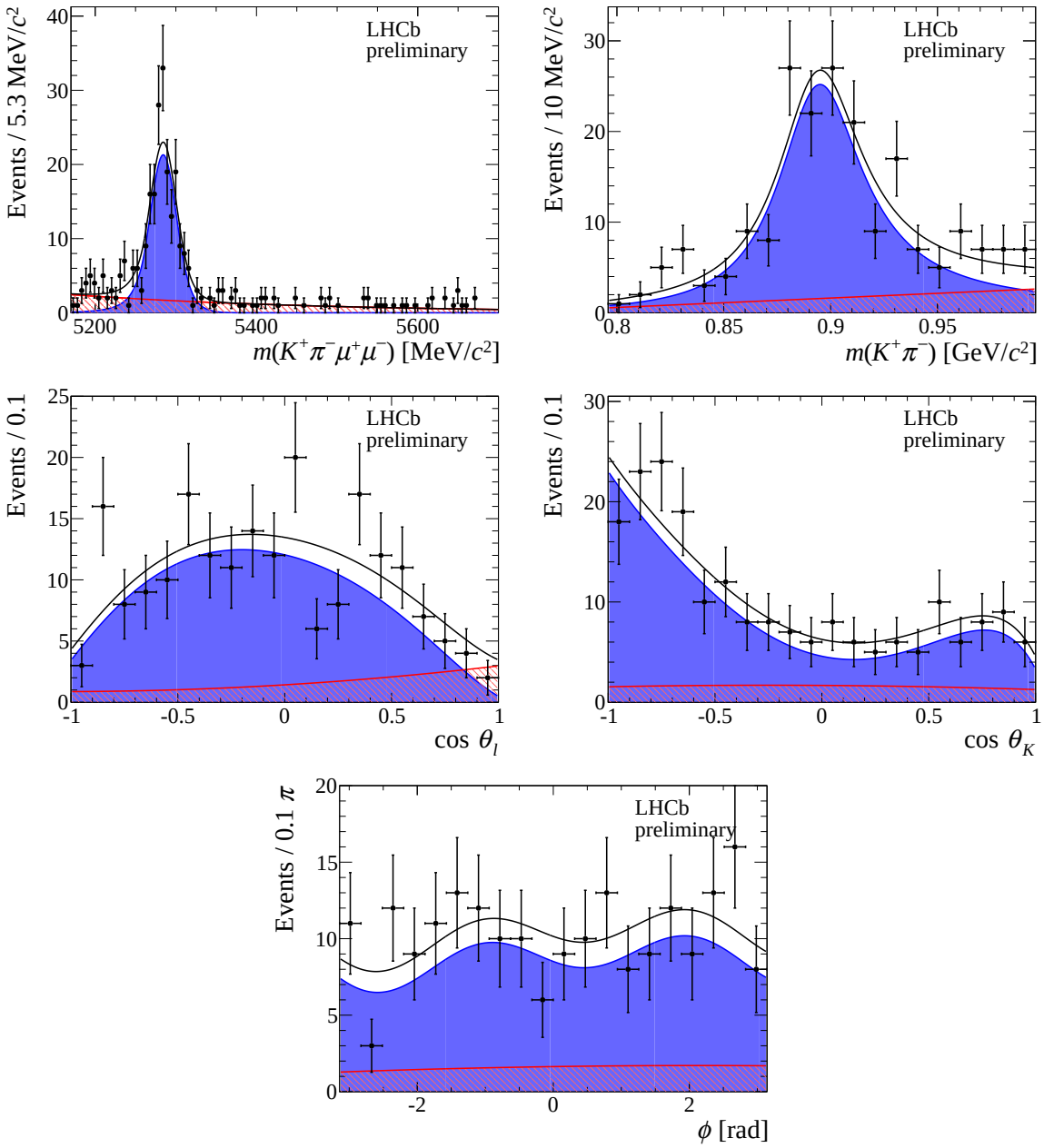

Figure 9: Angular and mass distributions for the q^2 bin $1.1 < q^2 < 2.5\,\mathrm{GeV}^2/c^4$. The $m(K^+\pi^-)$ distribution and the three decay angles are given in the signal mass window $\pm 50\,\mathrm{MeV}/c^2$ around the nominal B^0 mass. Overlaid are the projections of the total fitted distribution (black line) and its different components. The signal is shown by the blue component and the background is shown by the red hatched component.

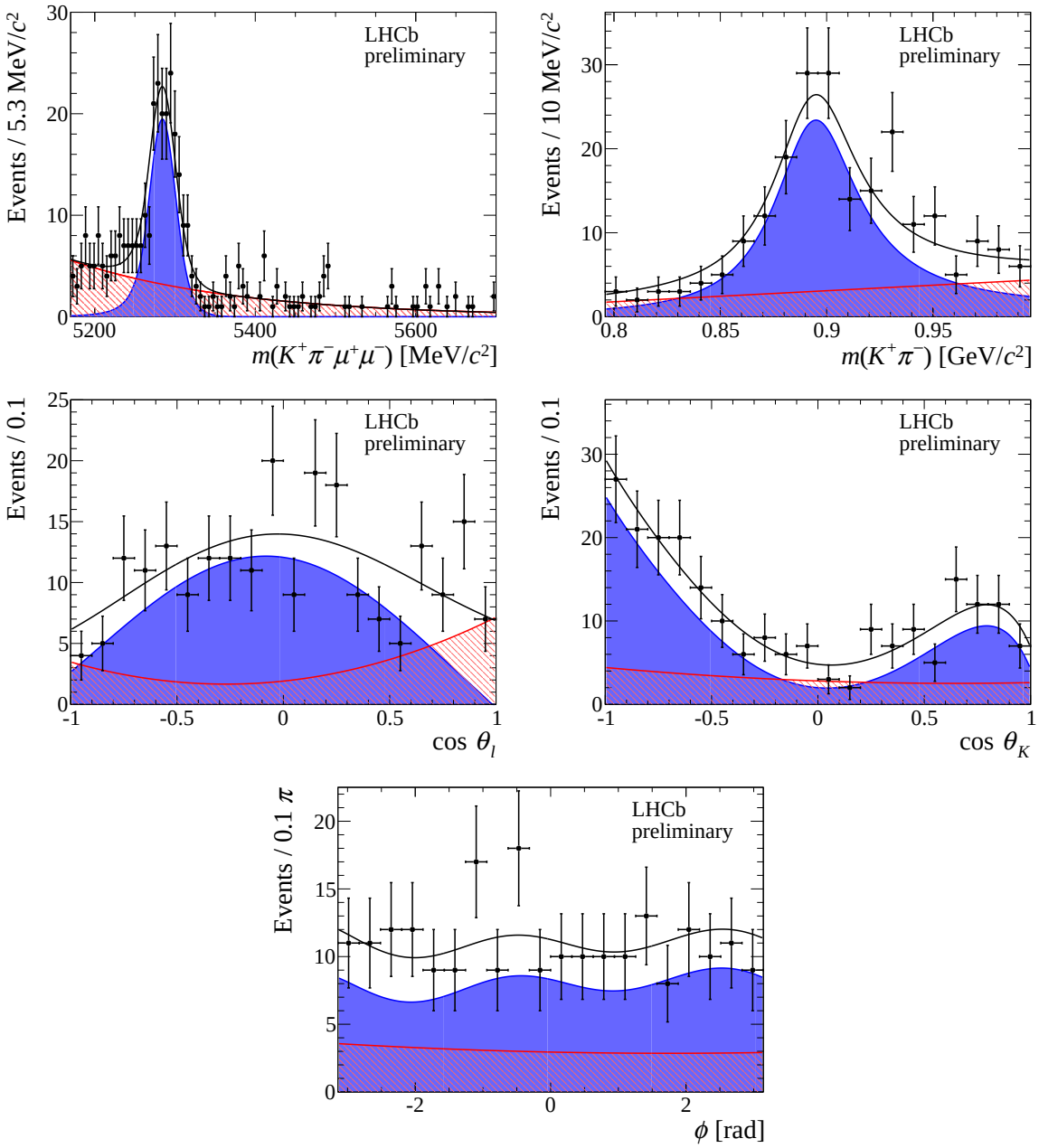

Figure 10: Angular and mass distributions for the q^2 bin $2.5 < q^2 < 4.0\,\mathrm{GeV}^2/c^4$. The $m(K^+\pi^-)$ distribution and the three decay angles are given in the signal mass window $\pm 50\,\mathrm{MeV}/c^2$ around the nominal B^0 mass. Overlaid are the projections of the total fitted distribution (black line) and its different components. The signal is shown by the blue component and the background is shown by the red hatched component.

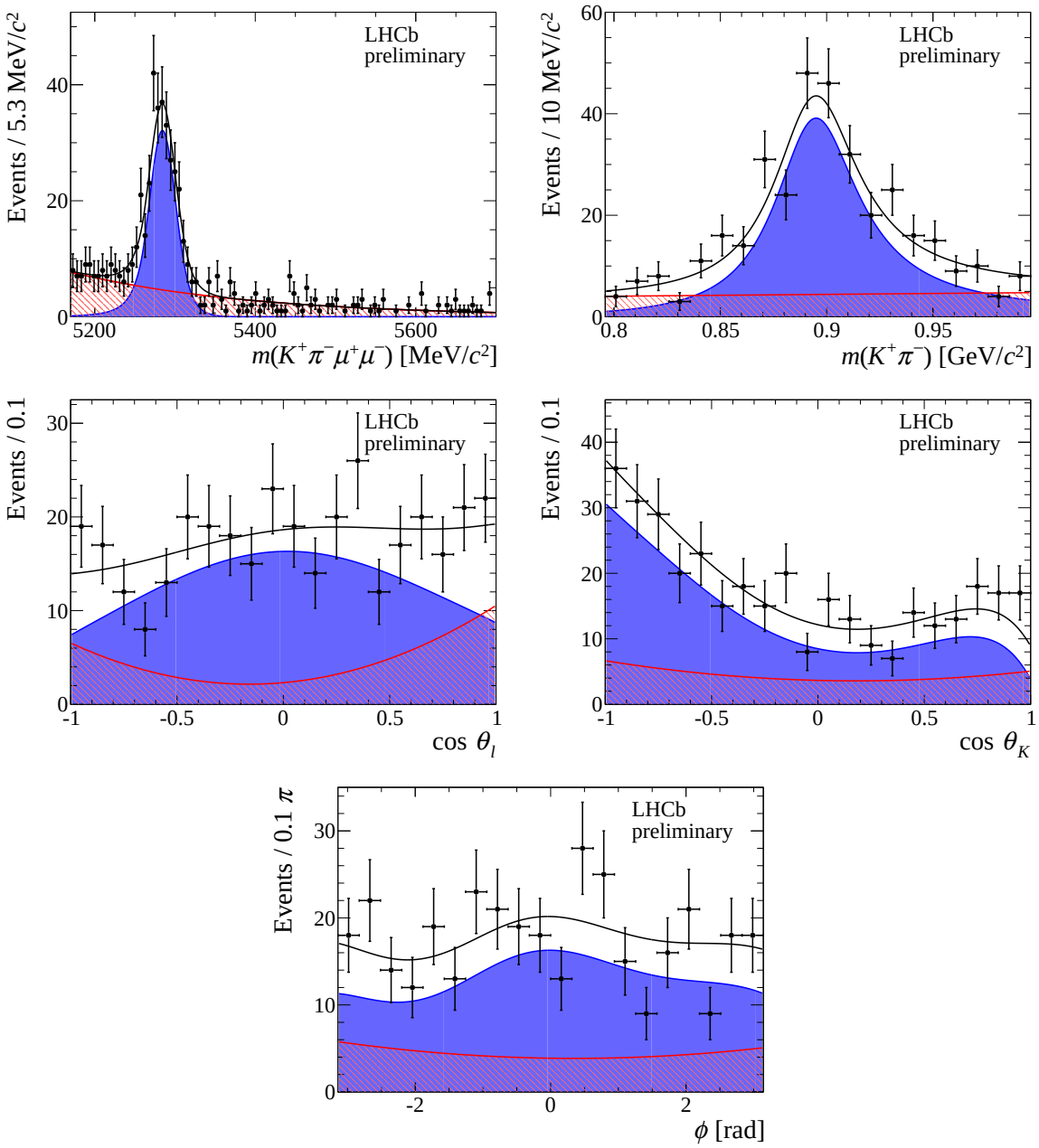

Figure 11: Angular and mass distributions for the q^2 bin $4.0 < q^2 < 6.0\,\mathrm{GeV}^2/c^4$. The $m(K^+\pi^-)$ distribution and the three decay angles are given in the signal mass window $\pm 50\,\mathrm{MeV}/c^2$ around the nominal B^0 mass. Overlaid are the projections of the total fitted distribution (black line) and its different components. The signal is shown by the blue component and the background is shown by the red hatched component.

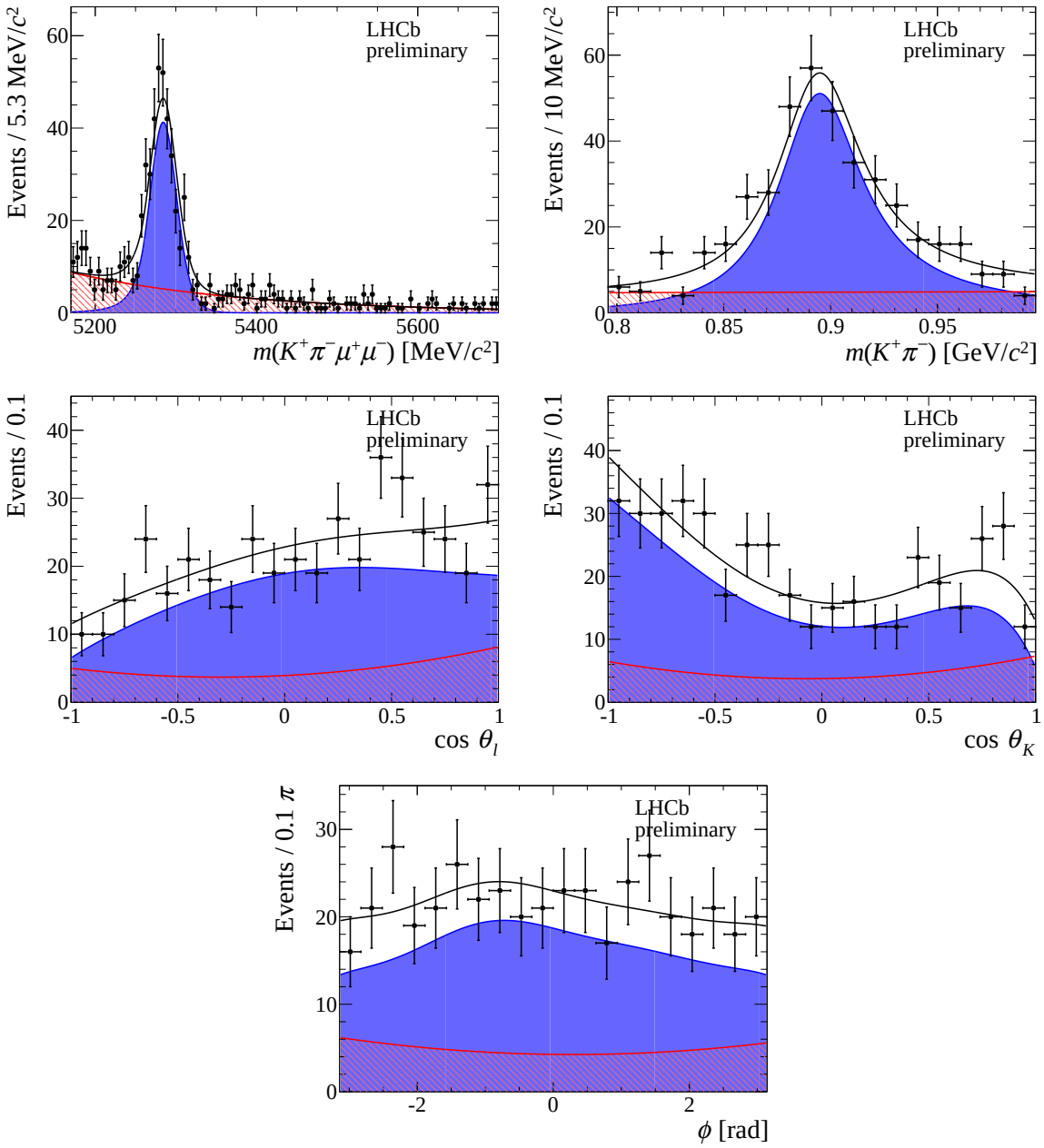

Figure 12: Angular and mass distributions for the q^2 bin $6.0 < q^2 < 8.0\,\mathrm{GeV}^2/c^4$. The $m(K^+\pi^-)$ distribution and the three decay angles are given in the signal mass window $\pm 50\,\mathrm{MeV}/c^2$ around the nominal B^0 mass. Overlaid are the projections of the total fitted distribution (black line) and its different components. The signal is shown by the blue component and the background is shown by the red hatched component.

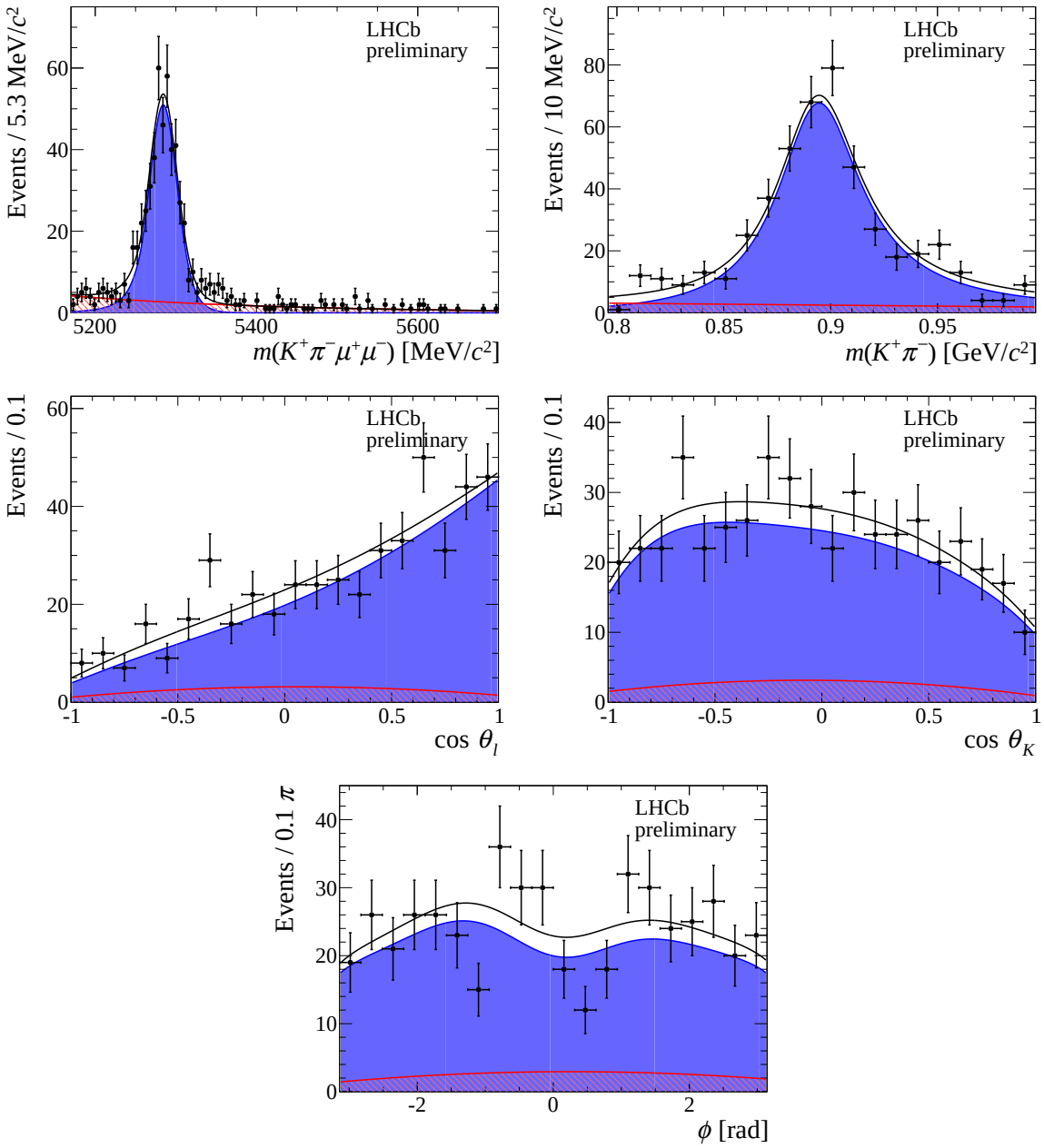

Figure 13: Angular and mass distributions for the q^2 bin $11.0 < q^2 < 12.5\,\mathrm{GeV}^2/c^4$. The $m(K^+\pi^-)$ distribution and the three decay angles are given in the signal mass window $\pm 50\,\mathrm{MeV}/c^2$ around the nominal B^0 mass. Overlaid are the projections of the total fitted distribution (black line) and its different components. The signal is shown by the blue component and the background is shown by the red hatched component.

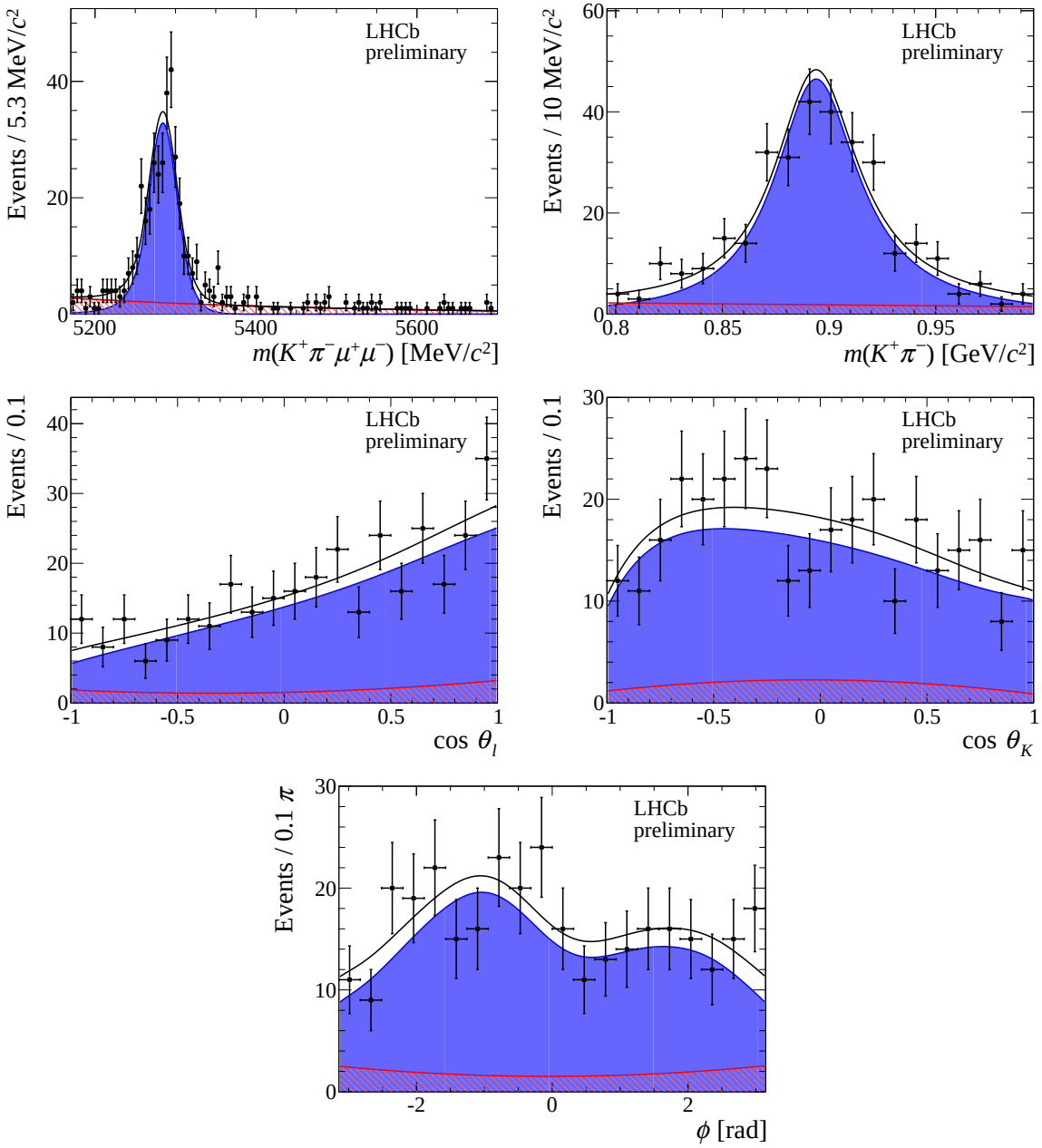

Figure 14: Angular and mass distributions for the q^2 bin $15.0 < q^2 < 17.0\,\mathrm{GeV}^2/c^4$. The $m(K^+\pi^-)$ distribution and the three decay angles are given in the signal mass window $\pm 50\,\mathrm{MeV}/c^2$ around the nominal B^0 mass. Overlaid are the projections of the total fitted distribution (black line) and its different components. The signal is shown by the blue component and the background is shown by the red hatched component.

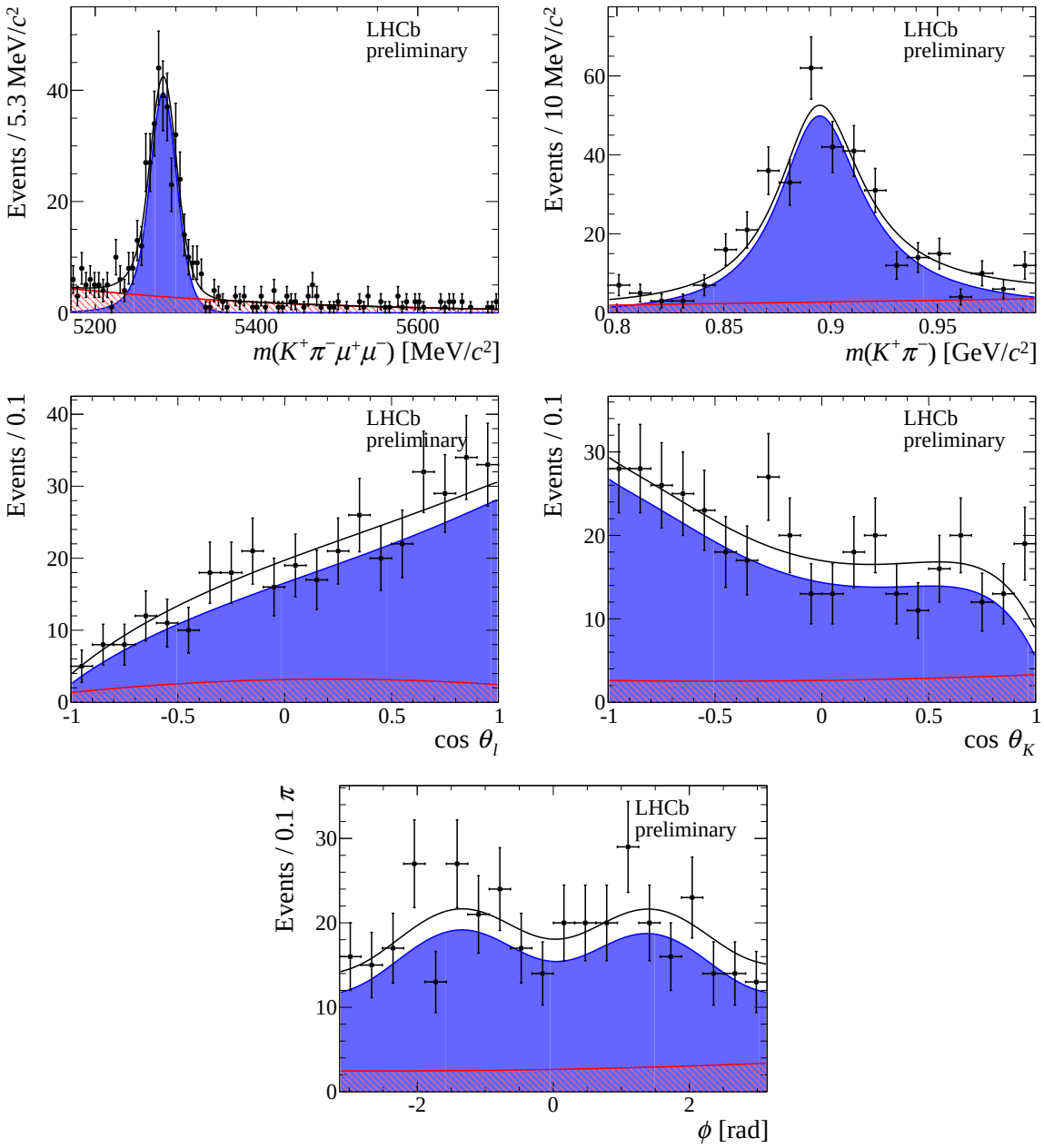

Figure 15: Angular and mass distributions for the q^2 bin $17.0 < q^2 < 19.0\,\mathrm{GeV}^2/c^4$. The $m(K^+\pi^-)$ distribution and the three decay angles are given in the signal mass window $\pm 50\,\mathrm{MeV}/c^2$ around the nominal B^0 mass. Overlaid are the projections of the total fitted distribution (black line) and its different components. The signal is shown by the blue component and the background is shown by the red hatched component.

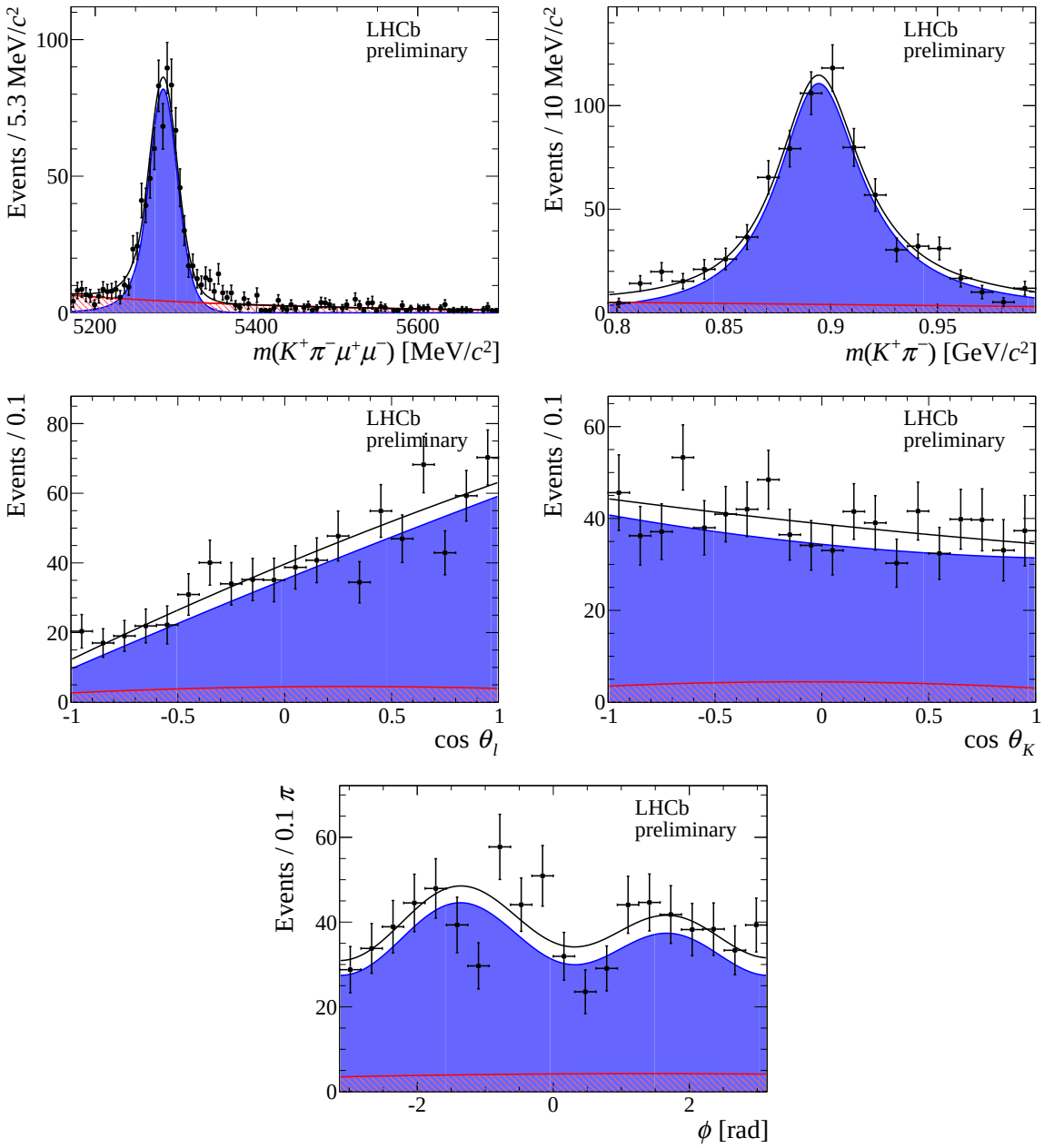

Figure 16: Angular and mass distributions for the q^2 bin $15.0 < q^2 < 19.0\,\mathrm{GeV}^2/c^4$. The $m(K^+\pi^-)$ distribution and the three decay angles are given in the signal mass window $\pm 50\,\mathrm{MeV}/c^2$ around the nominal B^0 mass. Overlaid are the projections of the total fitted distribution (black line) and its different components. The signal is shown by the blue component and the background is shown by the red hatched component.

C Correlation matrices

Correlation matrices between the observables in the different q^2 bins are provided below.

Correlation matrix $0.1 < q^2 < 0.98\,\mathrm{GeV}^2/c^4$

	F_L	S_3	S_4	S_5	A_FB	S_7	S_8	S_9
F_L	1.00	0.06	0.00	0.03	0.04	−0.02	0.07	0.08
S_3		1.00	0.01	0.10	−0.00	−0.07	−0.01	−0.03
S_4			1.00	0.08	0.11	−0.00	0.07	0.02
S_5				1.00	0.05	−0.01	0.00	0.04
A_FB					1.00	0.03	−0.07	0.02
S_7						1.00	0.01	0.11
S_8							1.00	0.02
S_9								1.00

Correlation matrix $1.1 < q^2 < 2.5\,\mathrm{GeV}^2/c^4$

	F_L	S_3	S_4	S_5	A_FB	S_7	S_8	S_9
F_L	1.00	0.09	0.07	0.07	0.09	−0.05	−0.04	0.08
S_3		1.00	−0.04	0.04	0.01	0.13	0.09	0.12
S_4			1.00	−0.22	−0.01	−0.00	−0.05	0.03
S_5				1.00	−0.14	−0.11	−0.03	−0.21
A_FB					1.00	−0.03	−0.10	−0.11
S_7						1.00	−0.11	0.23
S_8							1.00	−0.04
S_9								1.00

Correlation matrix $2.5 < q^2 < 4.0\,\mathrm{GeV}^2/c^4$

	F_L	S_3	S_4	S_5	A_FB	S_7	S_8	S_9
F_L	1.00	−0.13	−0.14	0.01	−0.03	0.10	−0.03	−0.01
S_3		1.00	−0.06	0.09	0.07	−0.02	0.01	−0.07
S_4			1.00	−0.19	−0.09	−0.05	0.12	0.07
S_5				1.00	−0.01	0.05	−0.02	0.10
A_FB					1.00	−0.01	−0.10	0.10
S_7						1.00	0.07	−0.05
S_8							1.00	−0.01
S_9								1.00

Correlation matrix $4.0 < q^2 < 6.0\,\mathrm{GeV}^2/c^4$

	F_L	S_3	S_4	S_5	A_FB	S_7	S_8	S_9
F_L	1.00	−0.03	0.09	0.10	−0.05	−0.10	0.04	0.00
S_3		1.00	−0.04	−0.03	0.09	−0.10	−0.00	−0.12
S_4			1.00	0.10	−0.10	−0.02	−0.04	0.04
S_5				1.00	−0.06	−0.03	−0.01	−0.04
A_FB					1.00	0.03	0.07	−0.03
S_7						1.00	0.06	−0.15
S_8							1.00	0.03
S_9								1.00

Correlation matrix $6.0 < q^2 < 8.0\,\mathrm{GeV}^2/c^4$

	F_L	S_3	S_4	S_5	A_FB	S_7	S_8	S_9
F_L	1.00	0.03	0.06	0.03	−0.31	−0.08	−0.01	−0.06
S_3		1.00	−0.16	−0.23	0.01	0.02	0.02	−0.07
S_4			1.00	−0.13	−0.12	−0.01	−0.11	0.01
S_5				1.00	−0.16	−0.14	−0.01	−0.04
A_FB					1.00	−0.01	0.04	0.02
S_7						1.00	0.10	−0.05
S_8							1.00	−0.10
S_9								1.00

Correlation matrix $11.0 < q^2 < 12.5\,\mathrm{GeV}^2/c^4$

	F_L	S_3	S_4	S_5	A_FB	S_7	S_8	S_9
F_L	1.00	0.25	0.02	−0.02	−0.62	0.03	0.05	0.02
S_3		1.00	0.05	−0.35	−0.24	−0.04	0.06	−0.02
S_4			1.00	−0.02	0.06	−0.05	−0.12	−0.08
S_5				1.00	0.01	−0.04	−0.09	−0.24
A_FB					1.00	−0.01	−0.06	0.07
S_7						1.00	0.27	−0.19
S_8							1.00	−0.09
S_9								1.00

Correlation matrix $15.0 < q^2 < 17.0\,\mathrm{GeV}^2/c^4$

	F_L	S_3	S_4	S_5	A_FB	S_7	S_8	S_9
F_L	1.00	0.26	−0.10	0.09	−0.50	−0.02	−0.06	0.14
S_3		1.00	−0.08	−0.03	−0.00	−0.04	−0.05	0.10
S_4			1.00	0.26	−0.16	−0.05	0.19	0.05
S_5				1.00	−0.20	0.12	−0.01	0.05
A_FB					1.00	0.05	−0.02	−0.08
S_7						1.00	0.25	−0.23
S_8							1.00	−0.11
S_9								1.00

Correlation matrix $17.0 < q^2 < 19.0\,\mathrm{GeV}^2/c^4$

	F_L	S_3	S_4	S_5	A_FB	S_7	S_8	S_9
F_L	1.00	0.07	0.06	0.04	−0.35	0.07	0.07	0.08
S_3		1.00	−0.15	−0.39	−0.05	−0.06	−0.04	−0.07
S_4			1.00	0.10	−0.17	0.03	0.18	−0.04
S_5				1.00	−0.11	0.04	0.01	−0.00
A_FB					1.00	−0.02	−0.09	−0.03
S_7						1.00	0.34	−0.15
S_8							1.00	−0.11
S_9								1.00

Correlation matrix $1.1 < q^2 < 6.0\,\mathrm{GeV}^2/c^4$

	F_L	S_3	S_4	S_5	A_FB	S_7	S_8	S_9
F_L	1.00	−0.04	0.05	0.03	0.05	−0.04	−0.01	0.08
S_3		1.00	−0.05	−0.00	0.05	0.01	0.01	−0.01
S_4			1.00	−0.05	−0.11	−0.02	−0.01	0.05
S_5				1.00	−0.07	−0.01	−0.02	−0.04
A_FB					1.00	0.02	−0.02	−0.04
S_7						1.00	0.04	−0.01
S_8							1.00	−0.03
S_9								1.00

Correlation matrix $15.0 < q^2 < 19.0\,\mathrm{GeV}^2/c^4$

	F_L	S_3	S_4	S_5	A_FB	S_7	S_8	S_9
F_L	1.00	0.17	−0.03	−0.02	−0.39	0.01	−0.00	0.11
S_3		1.00	−0.15	−0.19	0.05	−0.02	−0.04	−0.02
S_4			1.00	0.06	−0.12	0.03	0.14	0.01
S_5				1.00	−0.12	0.12	0.04	0.02
A_FB					1.00	0.00	−0.02	−0.01
S_7						1.00	0.24	−0.19
S_8							1.00	−0.13
S_9								1.00

D Comparison between $1\,\mathrm{fb}^{-1}$ and $3\,\mathrm{fb}^{-1}$ results

A comparison between the result obtained for P_5' in this note and the result from the $1\,\mathrm{fb}^{-1}$ LHCb analysis from Ref. [7] is shown in Fig. 17.

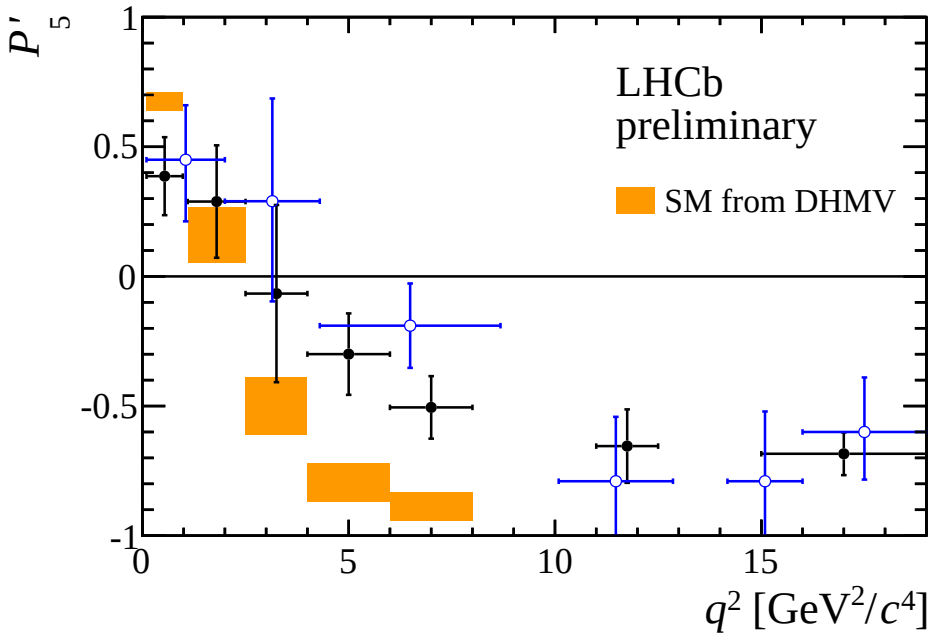

Figure 17: The observable P_5' in bins of q^2. The shaded boxes show the SM prediction taken from Ref. [13]. The blue open markers show the result of the $1\,\mathrm{fb}^{-1}$ analysis from Ref. [7].